Bioactive Materials 36 (2024) 524–540

Contents lists available at ScienceDirect

Bioactive Materials

journal homepage: www.keaipublishing.com/en/journals/bioactive-materials

A ROS-responsive hydrogel incorporated with dental follicle stem cell-derived small extracellular vesicles promotes dental pulp repair by ameliorating oxidative stress

Mengjie Li [a,b], Jun Tian [a,b], Kangkang Yu [c], He Liu [d], Xiaoqi Yu [e], Nan Wang [f], Qimei Gong [a,b,*], Kun Li [e,**], Ya Shen [d,***], Xi Wei [a,b,****]

[a] Hospital of Stomatology, Guanghua School of Stomatology, Sun Yat-Sen University, Guangzhou, China
[b] Guangdong Provincial Key Laboratory of Stomatology, Guangzhou, China
[c] Key Laboratory of Bio-resources and Eco-environment, Ministry of Education, College of Life Sciences, Sichuan University, Chengdu, China
[d] Division of Endodontics, Department of Oral Biological and Medical Sciences, The University of British Columbia, Vancouver, British Columbia, Canada
[e] Key Laboratory of Green Chemistry and Technology, Ministry of Education, College of Chemistry, Sichuan University, Chengdu, China
[f] Department of Pharmaceutical Engineering, College of Food and Bioengineering, Xihua University, Chengdu, China

ARTICLE INFO

Keywords:
Small extracellular vesicle
Dental follicle stem cell
Pulpitis
Oxidative stress
ROS-Responsive hydrogel

ABSTRACT

Pulpitis, an inflammatory disease of dental pulp tissues, ultimately results in the loss of pulp defense properties. Existing clinical modalities cannot effectively promote inflamed pulp repair. Oxidative stress is a major obstacle inhibiting pulp repair. Due to their powerful antioxidative capacity, mesenchymal stem cell-derived small extracellular vesicles (MSC-sEVs) exhibit potential for treating oxidative stress-related disorders. However, whether MSC-sEVs shield dental pulp tissues from oxidative damage is largely unknown. Here, we showed that dental follicle stem cell-derived sEVs (DFSC-sEVs) have antioxidative and prohealing effects on a rat LPS-induced pulpitis model by enhancing the survival, proliferation and odontogenesis of H_2O_2-injured dental pulp stem cells (DPSCs). Additionally, DFSC-sEVs restored the oxidative/antioxidative balance in DPSC mitochondria and had comparable effects on ameliorating mitochondrial dysfunction with the mitochondrion-targeted antioxidant Mito-Tempo. To improve the efficacy of DFSC-sEVs, we fabricated an intelligent and injectable hydrogel to release DFSC-sEVs by combining sodium alginate (**SA**) and the ROS sensor **RhB-AC**. The newly formed **SA-RhB** hydrogel efficiently encapsulates DFSC-sEVs and exhibits controlled release of DFSC-sEVs in a $HClO/ClO^-$ concentration-dependent manner, providing a synergistic antioxidant effect with DFSC-sEVs. These results suggest that DFSC-sEVs-loaded **SA-RhB** is a promising minimally invasive treatment for pulpitis by enhancing tissue repair in the pulp wound microenvironment.

1. Introduction

Pulpitis of permanent teeth is a common disease that usually causes pain and masticatory discomfort in patients and ultimately results in the loss of pulp defense properties [1]. The conventional treatment for pulpitis is root canal therapy (RCT), which involves the removal of all pulp tissue. However, the absence of pulp vitality is unfavorable for long-term tooth survival. When a pulpal lesion is localized or reversible, vital pulp therapy (VPT) is recommended to maximize the preservation of living pulp tissues. Compared with RCT, VPT is a less invasive and more cost-effective procedure for lowering the risk of fracture and tooth loss [1,2]. When performing VPT, pulp exposed to bacteria and their virulence factors needs to be carefully debrided and capped with appropriate materials to facilitate the formation of a hard tissue barrier. However, accurately identifying and debriding pulp lesions is quite challenging for clinicians, especially for junior dentists [3]. Such

Peer review under responsibility of KeAi Communications Co., Ltd.
* Corresponding authors. Hospital of Stomatology, Guanghua School of Stomatology, Sun Yat-Sen University, 56 Ling Yuan Xi Road, Guangzhou 510055, China.
** Corresponding author.
*** Corresponding authors.
**** Corresponding author. Hospital of Stomatology, Guanghua School of Stomatology, Sun Yat-Sen University, 56 Ling Yuan Xi Road, Guangzhou 510055, China.
E-mail addresses: gongqim@mail.sysu.edu.cn (Q. Gong), kli@scu.edu.cn (K. Li), yashen@dentistry.ubc.ca (Y. Shen), weixi@mail.sysu.edu.cn (X. Wei).

https://doi.org/10.1016/j.bioactmat.2024.06.036
Received 8 May 2024; Received in revised form 27 June 2024; Accepted 27 June 2024

technical difficulties will hinder clinicians from using VPT. More importantly, currently used calcium silicate-based capping materials such as MTA and iRoot BP Plus have been reported to have unfavorable effects on inflamed or infectious pulp, which is typically associated with the impairment of the self-repair capacity of dental pulp tissues [2,4]. Therefore, novel capping materials for treating pulpitis are demanded.

Secondary to bacterial infection, the injured pulp releases many proinflammatory mediators and maintains a high level of ROS, further weakening the repair capacity of the dental pulp. Notably, oxidative stress (OS) induced by abnormally elevated ROS levels can lead to cell death, decrease the osteogenic/odontogenic capacity of dental pulp stem cells (DPSCs) and exacerbate the inflammatory state [5,6]. Thus, OS has been proposed to strongly contribute to uncontrolled inflammation and delayed healing in various diseases. Previous studies have reported that the levels of ROS and the OS markers myeloperoxidase and 8-isoprostane are increased in pulpitis tissues [7,8]. Moreover, the use of exogenous antioxidants efficiently rescued the self-renewal and osteogenic differentiation abilities of OS-injured DPSCs *in vitro* [9]. These results suggested that regulating OS levels may be a potential strategy for inducing inflamed pulp repair. Currently, ROS-modulation treatments, including natural antioxidants, ROS-scavenging biomaterials, and antioxidant Nrf2 activators, have shown considerable efficacy in treating OS-related diseases, such as chronic skin wound injury, Parkinson's disease, and hepatic ischemia [10–12]. However, few studies have focused on therapeutic strategies targeting OS for pulpitis.

Recently, increasing evidence has demonstrated the antioxidative property of mesenchymal stem cell-derived small extracellular vesicles (MSC-sEVs). sEVs usually refer to bilayer membrane structures smaller than 200 nm in diameter that possess biological functions similar to those of their parental cells [13]. MSC-sEVs have been shown to exert considerable effects on a series of OS-related biological insults, including neurodegeneration, skin injury, and osteoarthritis [11,14]. The bioactive molecules in MSC-sEVs can be taken up by recipient cells, thus inhibiting oxidative stress and apoptosis in the lung, heart, brain, liver, skin and other cells and promoting survival and regeneration [14]. However, whether MSC-sEVs can protect DPSCs from OS-related damage and promote inflamed pulp repair *in vivo* is largely unknown.

Notably, unconjugated or free MSC-sEVs in the pathological environment cannot be retained for a long time [15]. Therefore, developing a drug scaffold that can serve as a sustained release carrier for MSC-sEVs is critical. Previously, we constructed an interpenetrating polymer network (IPN) hydrogel by combining sodium alginate (**SA**) and the ROS indicator **RhB-AC** [16]. As a biocompatible dressing material and a ROS scavenger, this IPN hydrogel exhibited excellent wound healing effects in a rat wound model. Based on prior research, the injectable hydrogel **SA-RhB** was designed to load DFSC-sEVs and intelligently release cargos by responding to ROS at the injured site, exerting synergistic effects on OS via DFSC-sEVs. Herein, we demonstrate the protective effect of DFSC-sEVs on OS-injured DPSCs and suggest that the DFSC-sEVs-loaded hydrogel system is a promising capping biomaterial for developing biological strategies to treat pulpitis.

2. Materials and methods

2.1. DFSCs and DPSCs isolation, culture and characterization

2.1.1. Isolation and culture of DFSCs/DPSCs

Rat DFSCs and DPSCs were isolated and cultured as previously described [17]. Briefly, dental follicles were separated from the mandibular molar tooth germ of Sprague–Dawley (SD) rats at postnatal day 7, and dental pulp tissues were separated from the maxillary incisors of 5-week-old male SD rats. The separated tissues were subsequently minced into small pieces, transferred to culture dishes and cultivated in α-minimum essential medium (α-MEM; Gibco, USA) supplemented with 20 % fetal bovine serum (FBS; Gibco, USA), 100 U/mL penicillin, and 100 mg/mL streptomycin (Gibco, USA). DFSCs and DPSCs were passaged at 80 %–90 % confluence, and cells from passages 3 to 5 were used for subsequent experiments.

2.1.2. Flow cytometric analysis of DFSCs/DPSCs

Surface marker profiles of DFSCs and DPSCs were identified via flow cytometric analysis. Cells in suspension were collected and stained with monoclonal antibodies against rat CD29-APC, CD34-FITC, and CD44/CD90/CD45-PE/FITC (all purchased from BioLegend, USA) for 30 min on ice. Then, the cells were washed twice and resuspended in PBS containing 1 % FBS for analysis by a flow cytometer (BD Biosciences, USA).

2.1.3. Induction of the osteogenic and adipogenic differentiation of DFSCs/DPSCs

DFSCs and DPSCs were seeded at a density of 2×10^5 cells/well in 6-well plates. The osteogenic differentiation of DFSCs and DPSCs was induced with osteogenic induction media for 21 days according to the manufacturer's instructions (Cyagen Biosciences, China), after which alizarin red staining was performed to visualize calcium deposits. Adipogenic differentiation was induced with adipogenic induction media for 21 days (Cyagen Biosciences, China), after which Oil Red O staining was used to identify lipid droplets.

2.2. Preparation and identification of DFSC-sEVs

DFSC-sEVs were isolated by differential ultracentrifugation as described previously [18]. In brief, 80 % confluent DFSCs were cultured in serum-free medium for 48 h, after which the supernatant was collected. After centrifugation at 800×*g* for 10 min and 3000×*g* for 10 min at 4 °C, the supernatant was centrifuged at 100,000×*g* for 70 min at 4 °C. The supernatant was subsequently discarded. DFSC-sEVs were resuspended in PBS and stored at −80 °C. The ultrastructure and size distribution of the purified DFSC-sEVs were determined using transmission electron microscopy (TEM) and nanoparticle tracking analysis (NTA). In addition, the specific sEV markers CD9, CD63 and TSG101 were examined by western blotting.

2.3. Western blotting

Total protein was extracted from DFSC-sEVs or DPSCs with RIPA lysis buffer, and the protein concentration was quantified via a BCA protein assay (Bocai, China). For Western blot analysis, 30 μg of protein was separated via SDS–polyacrylamide gel electrophoresis (SDS–PAGE; Invitrogen, USA) and transferred to 0.45-μm PVDF membranes. The membranes were then incubated for 1 h with 5 % bovine serum albumin (BSA; Sigma, USA) to block nonspecific binding, followed by incubation with primary antibodies at 4 °C overnight. Primary antibodies against CD9 (Affinity, China), CD63 (Affinity, China), TSG101 (Santa Cruz, USA) and MnSOD (Santa Cruz, USA) were used to assess protein expression. Then, the membranes were incubated with horseradish peroxidase-conjugated secondary antibodies (Cell Signaling Technology, USA) at room temperature for 1 h. The immunoreactive bands were detected via chemiluminescence (Millipore, USA).

2.4. Construction of a direct pulp capping model of rat pulpitis

The minimum sample size was calculated from our previous study [19]. Considering the possibility of sample loss, the final sample size in each group was 6. The direct pulp capping model of rat pulpitis was partially modified based on our previous experimental model [17]. Briefly, seven-to eight-week-old male SD rats were anesthetized via intraperitoneal injection of sodium pentobarbital (40 mg/kg). H_2O_2 (3 %) was used to disinfect the oral cavity, and 2.5 % sodium hypochlorite was used to disinfect the maxillary first molar. Then, the molar was drilled with a 1/4 round bur with cooling. Pulpal exposure was confirmed by the use of a 10-K file, which was carefully enlarged to a

40-K file using a 2.5 × dental surgical loupe. The exposed site was rinsed with 2.5 % sodium hypochlorite, 15 % EDTA and PBS. Then, 2 μL of 10 mg/mL *P. gingivalis* LPS (InvivoGen, France) was injected into the pulpal cavity. Then, for the LPS group and LPS + sEVs group, gelatin sponges soaked in 3 μL of PBS or 3 μL of DFSC-sEVs (2 μg/μL) were used to cap the exposed site. For the LPS + **SA-RhB** group and LPS + **SA-RhB**@sEVs group, 3 μL of DFSC-sEVs (2 μg/μL) unloaded/loaded in 3 μL of hydrogel was used as the capping material. iRoot BP Plus (Innovative BioCeramix, Canada) was applied to seal the pulp cavity. Then, the cavity was restored with adhesive resin (Shofu, Japan). At 3, 7 and 28 days post-treatment, the maxillae were collected and then fixed with 4 % paraformaldehyde for 24 h.

2.5. Micro-CT evaluation

The samples collected after 28 days were scanned by a micro-CT scanner (Scanco) with the following parameters: 70 kVp, 114 μA, 8 W and 10 μm voxel size. For each sample, the bone volume (BV) was measured and compared with the total volume (TV, BV/TV ratio) to evaluate the reparative effects beneath the exposed site.

2.6. Histological analysis

The samples were decalcified for 8 weeks, and paraffin-embedded sections were prepared for H&E staining and immunofluorescence staining. To assess the intensity of inflammatory infiltration, the density of inflammatory cells in the coronal pulp was graded based on an inflammation grading method that was applied in our previous study [19]. The four inflammation grades were as follows: no inflammation (score of 0), mild or slight inflammation (score of 1), moderate inflammation (score of 2), and severe inflammation and/or abscess formation (score of 3).

For teeth harvested at 3 d and 7 d, double staining for 8-OHdG/CD90 (Santa Cruz, USA) and single staining for DSPP (Affinity, China) were performed. Briefly, the samples were dewaxed, and antigen retrieval was conducted in citrate acid buffer by the microwave heating method. Then, the sections were blocked and permeabilized in 3 % BSA and 0.3 % Triton X-100 in PBS at room temperature for 1 h. Afterward, the samples were incubated with primary antibodies at 4 °C overnight and then incubated with a fluorescent-conjugated secondary antibody (Invitrogen, USA) at room temperature for 1 h. Finally, the sections were mounted with 4′,6-diamidino-2-phenylindole (DAPI)-containing mounting media (Invitrogen, USA) and examined by a laser-scanning confocal microscope (Olympus FV3000, Japan). The intensities of 8-OHdG and DSPP fluorescence were quantified using ImageJ.

2.7. Uptake of DFSC-sEVs by DPSCs

DPSCs were seeded in 24-well plates with cell-climbing slices at a density of 3×10^3 cells/well. DFSC-sEVs were labeled with PKH67 following the manufacturer's instructions (Sigma, USA), and PKH67-labeled DFSC-sEVs were subsequently incubated with DPSCs for 24 h. After fixation, the DPSC cytoskeleton was labeled with Alexa Fluor 555–conjugated phalloidin (Invitrogen, USA), and the nucleus was stained with DAPI. Cellular uptake of DFSC-sEVs was observed via confocal microscopy.

2.8. OS injury model in vitro

To simulate the OS microenvironment, DPSCs were exposed to 50–700 μM H_2O_2 for 6 h. Then, H_2O_2-injured DPSCs were subjected to regular culture medium for 24 h. Cell viability was evaluated by Cell Counting Kit-8 assays (CCK-8; GlpBio, USA) according to the manufacturer's instructions.

2.9. Evaluation of oxidative and antioxidative states

To evaluate the protective effects of DFSC-sEVs on OS-injured DPSCs, DPSCs were pretreated with 40 μg/mL DFSC-sEVs for 24 h and then stimulated with 200 μM H_2O_2 for 6 h.

2.9.1. Measurement of intracellular ROS levels

The intercellular ROS levels were measured by a ROS assay kit (Phygene, China). H_2O_2-injured DPSCs were incubated with 10 μM DCFH-DA at 37 °C for 30 min. Afterward, the DPSCs were digested and resuspended in PBS. ROS were quantified by flow cytometry.

2.9.2. Measurement of malondialdehyde (MDA) and superoxide dismutase (SOD) levels

MDA is an indicator of lipid peroxidation, and SOD activity reflects the antioxidant activity of samples. Cells were collected, lysed by sonication and centrifuged at 8000×*g* for 10 min at 4 °C. The supernatants were harvested and placed on ice for the assays. MDA and SOD activities were measured using assay kits (Solarbio, China) according to the manufacturer's instructions.

2.9.3. Immunofluorescence staining for 8-OHdG

8-OHdG is used to evaluate the level of DNA oxidative damage. After fixation, blocking and permeabilization, DPSCs on cell-climbing slices were incubated with an anti-8-OHdG primary antibody (Santa Cruz, USA) and then incubated with an Alexa Fluor-488-conjugated secondary antibody (Invitrogen, USA) as previously described. Fluorescence images were captured by a confocal microscope.

2.10. BrdU assay

After H_2O_2 stimulation with or without DFSC-sEVs pretreatment, the used culture media were changed to regular culture media containing 10 μM BrdU for 6 h. To evaluate BrdU incorporation, the cells were incubated with an anti-BrdU primary antibody (Servicebio, China) and subsequently stained with a fluorescent-conjugated secondary antibody as previously described. The $BrdU^+$ cells were observed by confocal microscopy and quantified using NIH ImageJ software.

2.11. Apoptosis assay

DPSCs were harvested and resuspended in 100 μL of binding buffer and then incubated with 2.5 μL of Annexin V-FITC and 2.5 μL of 7-AAD for 20 min. The staining was terminated with 400 μL of binding buffer. The percentage of apoptotic DPSCs was detected via flow cytometry analysis.

2.12. Quantitative real-time polymerase chain reaction (qRT–PCR)

Total RNA was isolated from H_2O_2-treated DPSCs using an RNA quick purification kit (ESscience, China), and complementary DNA (cDNA) was prepared using a cDNA synthesis kit (Yeasen, China). qRT–PCR was conducted with SYBR Green Master Mix (Yeasen, China). The primers used in the PCRs are listed in Supplementary Table S1. The values are reported as relative mRNA expression levels and were calculated using the $2^{-\Delta\Delta CT}$ comparative method, and β-actin served as the control.

2.13. RNA sequencing

Small RNAs were extracted from DPSCs treated with H_2O_2 or H_2O_2 +sEVs for RNA sequencing. RNA sequencing was performed using the BGISEQ-500 platform (BGI, China), and the RNA was analyzed on a network platform (https://biosys.bgi.com/). Genes with a fold change$\geq|2|$ and a q value < 0.5 were considered differentially expressed genes (DEGs).

2.14. Mitochondrial profile analysis

To evaluate mitochondrial mass and mitochondrial ROS (mtROS) levels, MitoTracker Green and MitoSOX (for mtROS) staining were performed according to the manufacturer's instructions (Invitrogen, USA). The cells were collected and analyzed using a flow cytometry system. To evaluate the mitochondrial membrane potential (MMP), DPSCs were stained with 5 μM JC-1 for 15 min. After washing 3 times with PBS, fluorescence images were captured via an inverted fluorescence microscope (Zeiss, Germany). To evaluate mitochondrial DNA (mtDNA) oxidative damage, DPSCs were incubated with 300 nM MitoTracker Deep Red for 30 min. Then, immunofluorescence staining for 8-OHdG was conducted as previously described.

2.15. Preparation and characterization of the ***SA-RhB*** hydrogel

2.15.1. Synthesis and characterization of the ***RhB-AC*** monomer

The monomer **RhB-AC** was synthesized as a ROS-responsive fluorescence sensor based on our previous work [16]. Biologically reactive oxygen species, including O_2^-, H_2O_2, HClO/ClO^-,·OH, ONOO- and ^{t}BuOOH, were prepared, and the fluorescence response of **RhB-AC** toward various ROS was evaluated via fluorescence spectroscopy (HITACHI, Japan).

2.15.2. Preparation of the ***SA-RhB*** hydrogel

To improve the biocompatibility of the hydrogel, sodium alginate (**SA**) was chosen to construct an IPN combined with **RhB-AC**. **SA** can crosslink rapidly with Ca^{2+} to form a gel. To delay the gelation time of **SA**, Na_2HPO_4 was introduced as a retardant regent to interact with the Ca^{2+} source to produce calcium phosphate. Then, 60 μL of 0.1 M, 0.3 M, 0.5 M, 0.7 M or 0.9 M Na_2HPO_4 was added to the crosslinking reaction mixture. The details for preparing **SA-RhB** are shown in Supplementary Table S2. The gelation time was determined using the tube inversion method, and the injectability of **SA-RhB** was confirmed by extruding the solution from a 1-mL syringe.

2.15.3. Morphological structure of ***SA-RhB***

After gelation, the **SA** and **SA-RhB** samples were frozen in liquid nitrogen and lyophilized for 48 h. The internal structures of the gels were examined by scanning electron microscopy (SEM).

2.15.4. Swelling test

Cylindrical samples with a diameter of 7 mm and a height of 5 mm were immersed in 5 mL of PBS and incubated at 37 °C for 6 h. At each time point, the weights of the samples were recorded as W_t. Before weighing, the surface of the gel was gently dried with filter paper. The swelling ratio was calculated as follows:

$$\text{swelling ratio} = \frac{Wt - W0}{W0} \times 100\%, \text{where } W_0 \text{ refers to the initial weight of the hydrogel.}$$

2.15.5. Degradation test

Cylindrical samples were submerged in 5 mL of PBS containing different concentrations of HClO/ClO^- and EDTA. The samples were incubated at 37 °C on a shake plate at 100 r.p.m. Photos were taken at each time point, and the trigger solutions were replaced daily until the gel was thoroughly degraded.

2.15.6. HClO/ClO^- response

Cylindrical samples were soaked in 5 mL of PBS or HClO/ClO^- solution (ethanol/PBS = 1:9, v/v) at 50 μM, 100 μM, 200 μM, 500 μM, or 1000 μM. The samples were incubated at 37 °C on a shake plate at 100 r.p.m. The media were photographed under UV 365 nm at each time point, and the fluorescence intensity was detected via fluorescence spectroscopy.

2.15.7. Cytotoxicity assay

The trigger solutions were collected and dialyzed using dialysis tubes (MWCO, 3000 Da). After lyophilization, the degradation products were obtained. DPSCs were incubated in culture media supplemented with different concentrations of degradation products for 1 d, 2 d or 3 d. Cell Counting Kit-8 (CCK-8) assays (GlpBio, USA) and live/dead staining (Bestbio, China) were conducted according to the manufacturers' instructions.

2.15.8. Encapsulation and release of ***SA-RhB***-loaded DFSC-sEVs

PKH67-labeled DFSC-sEVs were mixed with **SA-RhB** solution. Then, the solution was injected into a confocal dish. After gelation, the 3D structure of the gel was rebuilt using a Z-stack and a confocal microscope.

Cylindrical samples encapsulated with 300 μg of DFSC-sEVs were prepared. The samples were soaked in 5 mL of PBS or 100 μM, 500 μM, or 1000 μM HClO/ClO^- solution. The medium was replaced daily, and the protein concentration (C_t) was determined via a BCA protein assay. The percentage of cumulative DFSC-sEV release was calculated as follows:

$$\text{Percentage} = \frac{(C1 + C2 + \ldots + Ct) \times 5}{300} \times 100$$

2.16. Statistical analysis

Each experiment was repeated at least three times. The data are presented as the mean ± standard deviation and were analyzed using GraphPad Prism software. After the normality test and homogeneity of variance test, one-way ANOVA or the Kruskal–Wallis test was chosen, followed by Tukey's post hoc test or Dunnett's *t*-test. $P < 0.05$ indicated statistical significance.

3. Results

3.1. Characterization of DPSCs, DFSCs and DFSC-sEVs

As shown in Fig. S1A, flow cytometry revealed that both DPSCs and DFSCs highly expressed typical MSC surface markers, including CD29, CD44 and CD90, with frequencies up to 96.8 %, but rarely expressed CD34 and CD45, with frequencies less than 0.11 %. Furthermore, alizarin red staining revealed calcified deposits, and Oil Red O staining revealed lipid droplets in both DPSCs and DFSCs (Figs. S1B and C). These results demonstrated that cultured DPSCs and DFSCs exhibited the mesenchymal phenotype of MSCs, along with their multipotent differentiation capacity.

TEM and NTA revealed that the nanoparticles derived from DFSCs had a round shape, a membrane bilayer morphology and an average diameter of 163 nm (Fig. 1A and B). In addition, Western blot analysis of DFSC-sEVs revealed the presence of classical sEV markers, including CD9, CD63 and TSG101 (Fig. 1C). These results confirmed that DFSC-sEVs were successfully isolated.

3.2. DFSC-sEVs alleviate oxidative stress and promote dentin defect repair in inflamed pulp

First, we confirmed the protective effect of DFSC-sEVs using a LPS-induced pulpitis model. Histological analysis of the cells revealed that LPS-elicited inflammatory cells accumulated beneath the exposed site after 3 days and that this effect was attenuated by the administration of DFSC-sEVs (Fig. 1D). Inflammation grading also revealed that during the same duration, the inclusion of DFSC-sEVs decreased the severity of LPS-induced inflammation (Fig. S2A). With time, inflammatory infiltration generally decreased in both the LPS and LPS + sEVs groups. At 28 d posttreatment, the LPS group exhibited irregular calcification and disorganized pulp tissues at the exposed site, while the LPS + sEVs group

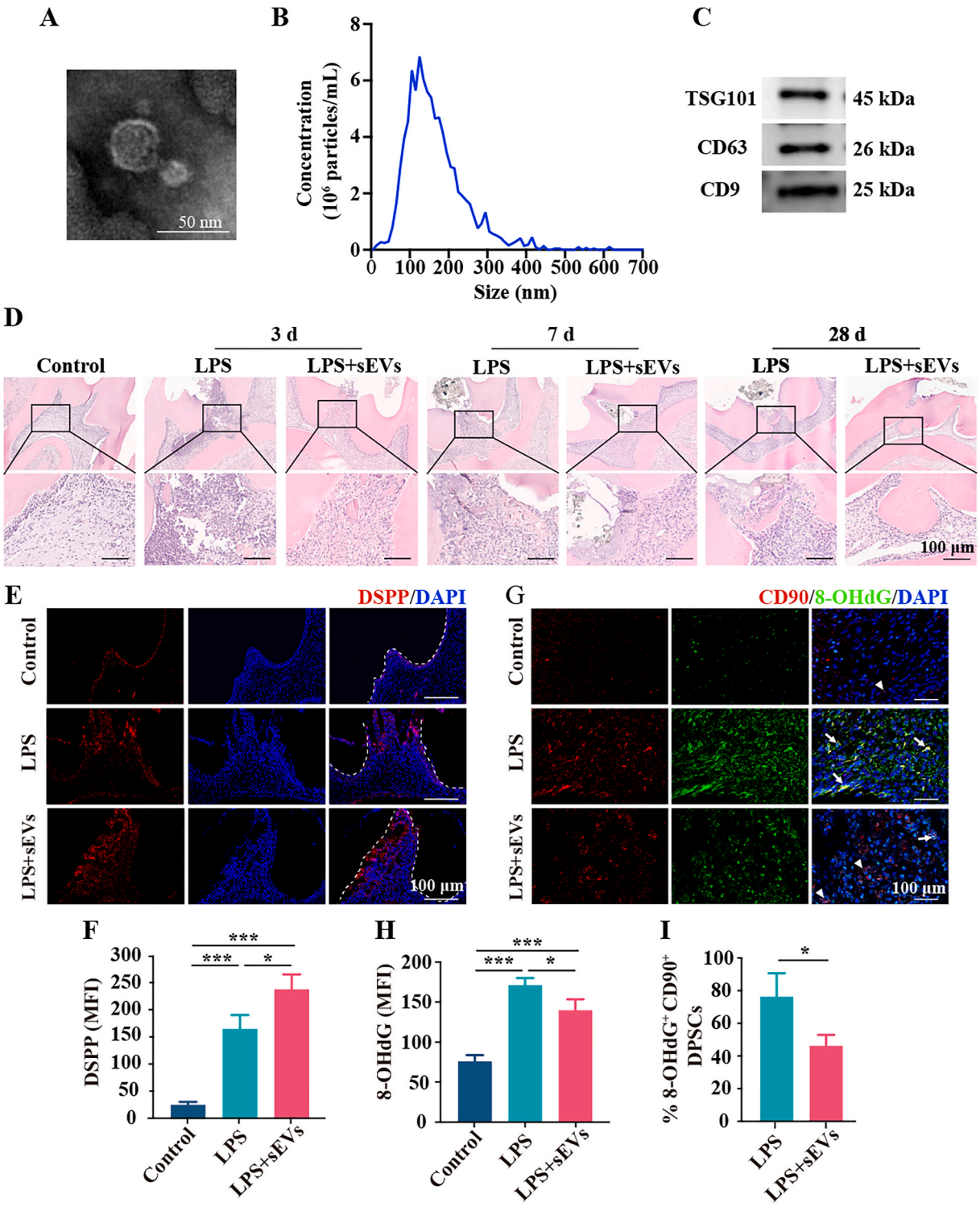

Fig. 1. Antioxidant and prohealing effects of DFSC-sEVs on LPS-induced rat pulpitis. (A) TEM image of DFSC-sEVs. (B) The size distribution of DFSC-sEVs was measured via nanoparticle tracking analysis (NTA). (C) Western blot analysis of the sEV-specific proteins CD9, CD63, and TSG101. (D) Representative images of HE staining in the control, LPS and LPS + sEVs groups at 3, 7 and 28 d after the operation. (E) DSPP immunofluorescence staining at the exposed pulp site 7 d after the operation. The white dashed lines indicate the junction between the dentin and dental pulp. (F) Semiquantitative analysis of DSPP levels. (G) Immunofluorescence staining for 8-OHdG and $CD90^+$ DPSCs at the site of pulp injury 3 d after the operation. The arrows indicate $CD90^+$ DPSCs, and the arrowheads indicate 8-$OHdG^+CD90^+$ DPSCs. (H) Semiquantitative analysis of 8-OHdG levels. (I) The percentage of $CD90^+$ DPSCs that experienced oxidative stress among the groups. MFI, mean fluorescence intensity. $^{***}P < 0.001$, $^{*}P < 0.05$.

presented a large range of mineralized tissue barriers and relatively normal pulp under the barrier (Fig. 1D). In addition, micro-CT scanning also demonstrated that the volume of the mineralized tissue barrier was significantly greater in the LPS + sEVs group than in the LPS group (Figs. S2B and C). The expression of DSPP, a marker of dentin mineralization, significantly increased after 7 d of LPS treatment, and the incorporation of DFSC-sEVs resulted in greater DSPP expression than that in the LPS group (Fig. 1E and F). Moreover, after 3 d of LPS stimulation, the expression of 8-OHdG, a typical marker of DNA oxidative damage, was strongly upregulated in LPS-injured pulp, indicating the occurrence of pronounced OS in LPS-treated pulp (Fig. 1G and H). In addition, we labeled DPSCs with CD90, and a substantial increase in 8-OHdG^{+} CD90^{+} cells was observed in the inflamed pulp, suggesting that the DPSCs recruited to the coronal pulp were affected by OS (Fig. 1I). However, DFSC-sEVs significantly alleviated OS and decreased the proportion of 8-OHdG^{+}CD90^{+} cells (Fig. 1G–I). Taken together, these results indicated that OS was widespread in LPS-induced pulpitis and that DFSC-sEVs could promote the healing potential of inflamed pulp, an effect partly dependent on their antioxidative effects on DPSCs.

3.3. DFSC-sEVs exert an antioxidative effect on H_2O_2-damaged DPSCs

To further confirm the protective effect of DFSC-sEVs on DPSCs against OS *in vitro*, H_2O_2 was used to induce oxidative damage in DPSCs. CCK8 assays showed that H_2O_2 significantly reduced the viability of DPSCs in a dose-dependent manner. In the subsequent experiment, 200 μM H_2O_2 was chosen to simulate OS in DPSCs, which led to a decrease in cell viability to almost 60 % in 24 h (Fig. 2A). The uptake of PKH67-labeled DFSC-sEVs by DPSCs was visualized using confocal microscopy (Fig. 2B). As expected, pretreatment with DFSC-sEVs significantly decreased the intracellular ROS levels and reduced the expression of the OS damage markers MDA and 8-OHdG in H_2O_2-stimulated DPSCs (Fig. 2C–G). Additionally, SOD activity was considerably higher in the H_2O_2+sEVs group than in the H_2O_2 group (Fig. 2H). These results indicated that DFSC-sEVs normalized the oxidative and antioxidative balance of DPSCs.

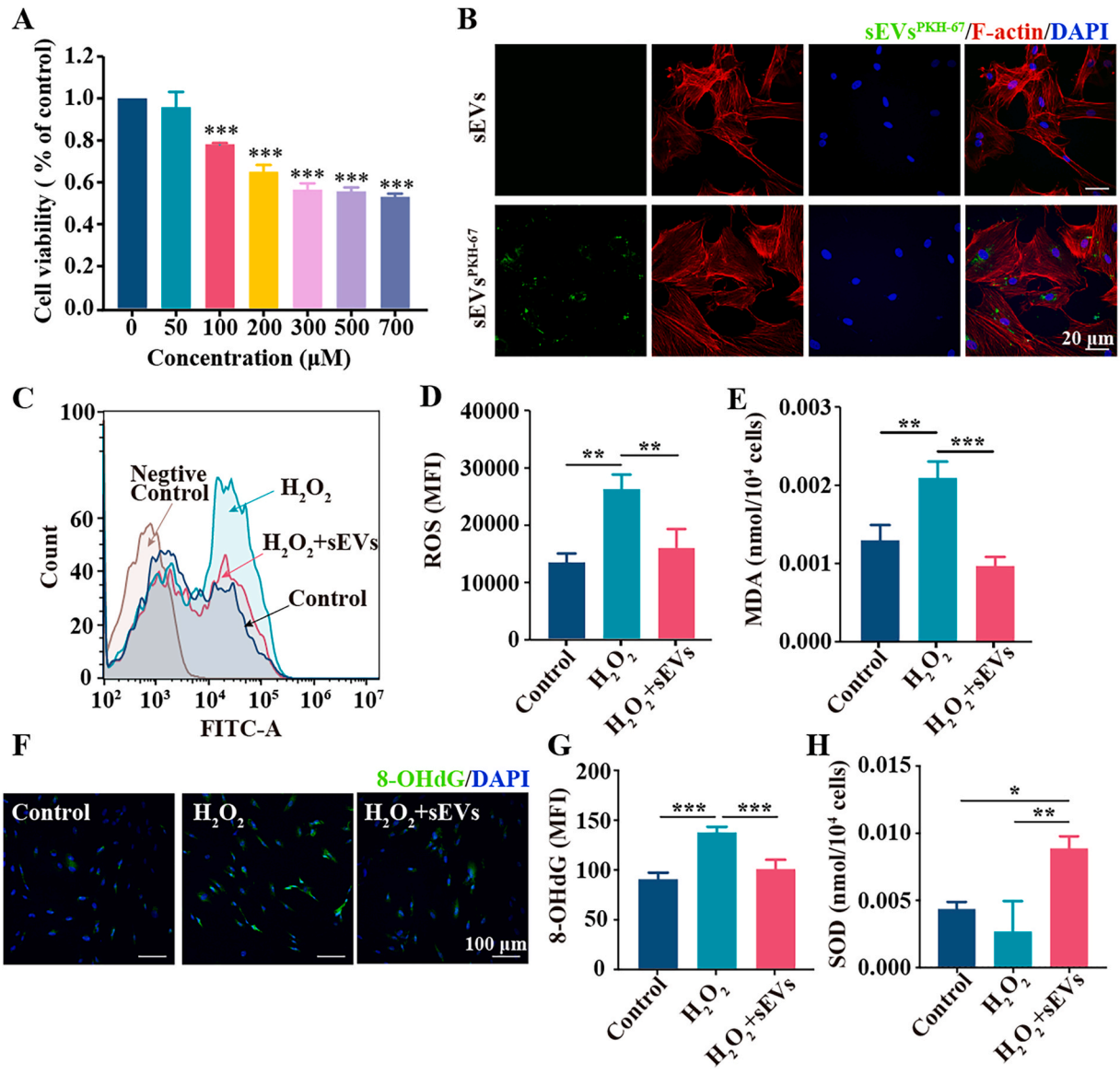

Fig. 2. DFSC-sEVs exerted antioxidative effects on H_2O_2-damaged DPSCs. (A) CCK-8 assay showing DPSCs viability at 24 h after 6 h of H_2O_2 stimulation. (B) Uptake of PKH67-labeled DFSC-sEVs by DPSCs at 24 h. (C, D) Intracellular ROS levels in DPSCs were determined using the agent DCFH-DA. (E) MDA levels in DPSCs were detected via a MDA assay. (F, G) 8-OHdG immunofluorescence staining of DPSCs. (H) SOD activity in DPSCs measured with the SOD assay. MFI, mean fluorescence intensity. ***$P < 0.001$, **$P < 0.01$, *$P < 0.05$.

Sustained OS leads to cell death and affects MSCs differentiation. Since the survival, proliferation and odontogenic differentiation of DPSCs are essential prerequisites for the pulpal wound healing process, we next investigated the effects of DFSC-sEVs on these biological processes in H_2O_2-damaged DPSCs. H_2O_2 significantly promoted DPSC apoptosis and reduced the number of BrdU $^+$ DPSCs, effects that were rescued by DFSC-sEVs (Fig. 3A–D). Furthermore, fewer mineralized modules and lower expression of odontogenic marker genes, including *Alpl* (encoding ALP), *Ibsp* (encoding BSP) and *Dcn* (encoding DCN), were observed in the H_2O_2 group than in the control group. Notably, DFSC-sEVs partially rescued the osteogenic/odontogenic differentiation potential of H_2O_2-treated DPSCs (Fig. 3E and F). In contrast, H_2O_2 stimulation promoted the formation of lipid droplets and dramatically upregulated the expression of adipogenic marker genes, including *Cfd* (encoding adipsin), *Cebpa* (encoding CEBPα) and *Cebpb* (encoding CEBPβ), and DFSC-sEVs effectively suppressed the adipogenic differentiation of H_2O_2-stimulated DPSCs (Fig. 3G and H). These results revealed that DFSC-sEVs enhanced the survival, proliferation and osteogenesis/odontogenesis of H_2O_2-injured DPSCs.

3.4. DFSC-sEVs protect H_2O_2-damaged DPSCs by ameliorating mitochondrial dysfunction

Mitochondria are major sources of ROS and predominant targets of OS, thus, the protective effect of DFSC-sEVs on DPSC mitochondria was assessed. Using the mitochondria-specific ROS indicator MitoSOX to determine mtROS levels in DPSCs, we found that mtROS were overproduced in response to H_2O_2 and that this change could be reversed by either DFSC-sEVs or Mito-Tempo, a mitochondrial superoxide scavenger. Specifically, the ability of DFSC-sEVs to inhibit mtROS production was nearly the same as that of Mito-Tempo (Fig. 4A and B). The overproduction of mtROS may disrupt mitochondrial function, manifesting mainly as an increase in the mitochondrial mass, a decrease in the mitochondrial membrane potential (MMP) and a decrease in ATP production. Therefore, we used MitoTracker Green probes to assess mitochondrial mass. Compared with that in control DPSCs, the fluorescence intensity of MitoTracker Green was higher in H_2O_2-treated DPSCs, and DFSC-sEVs and Mito-Tempo significantly inhibited mitochondrial mass abnormalities (Fig. 4C). The MMP was also evaluated in DPSCs using JC-1 dye. H_2O_2 stimulation caused a significant increase in the JC-1 aggregate/monomer ratio, indicating that MMP dissipation occurred in DPSCs. However, the MMP impairment was successfully reversed by treatment with DFSC-sEVs or Mito-Tempo (Fig. 4D and E). Furthermore, both DFSC-sEVs and Mito-Tempo significantly promoted ATP production in H_2O_2-injured DPSCs (Fig. 4F).

mtROS overproduction can impair mitochondrial function by destabilizing the mitochondrial oxidative/antioxidative balance. 8-OHdG staining was combined with MitoTracker Deep Red staining to visualize oxidized mtDNA and evaluate mitochondrial oxidative damage. We found that H_2O_2 treatment increased the colocalization of 8-OHdG and MitoTracker Deep Red, an effect that was reversed by DFSC-sEVs and Mito-Tempo (Fig. 4G). We also explored whether DFSC-sEVs improved the antioxidation capacity of DPSCs. Western blot analysis of H_2O_2-treated DPSCs revealed that DFSC-sEVs, like Mito-Tempo, upregulated the expression of MnSOD, a powerful antioxidant confined to mitochondria (Fig. 4H and I). These results indicated that DFSC-sEVs positively regulated the balance between mitochondrial oxidation and antioxidation, leading to restored mitochondrial function.

Since mitochondria play an important role in determining the fate of MSCs, we next assessed whether DFSC-sEVs enhance the survival and proliferation of H_2O_2-injured DPSCs and restore their odontogenic differentiation capacity by alleviating mitochondrial OS. After mitochondrial OS was attenuated by Mito-Tempo, H_2O_2-treated DPSCs exhibited decreased apoptosis and increased proliferation (Fig. 5A–D). In addition, the impaired odontogenic differentiation and elevated adipogenic differentiation of H_2O_2-stimulated DPSCs were reversed by Mito-Tempo (Fig. 5E–H). Notably, the protective effects of DFSC-sEVs were statistically indistinguishable from those of Mito-Tempo. The above findings suggested that DFSC-sEVs could protect DPSCs from OS by ameliorating mitochondrial dysfunction.

3.5. DFSC-sEVs mediate transcriptional changes in H_2O_2-stimulated DPSCs

Next, RNA sequencing was applied to assess the transcriptomic changes in DPSCs in the presence of H_2O_2 or H_2O_2+sEVs. In total, 2271 DEGs were identified between the H_2O_2-treated group and the control group, including 1460 upregulated genes and 811 downregulated genes (Fig. S3A). GO analysis and GSEA revealed that the intrinsic apoptotic signaling pathway in response to DNA damage, negative regulation of cell proliferation, cellular response to hydrogen peroxide and DNA repair were involved in the response to H_2O_2 stimulation, and mitochondrial protein import and transcriptional activation of mitochondrial biogenesis were enriched in the control group (Figs. S3B and C). In addition, a total of 54 genes were differentially expressed between the H_2O_2 group and H_2O_2+sEVs group. After removing 16 unannotated genes, a heatmap was generated to visualize the expression of 38 genes among the three groups (Fig. 6A). Specifically, MnSOD/SOD2 expression was significantly elevated in the H_2O_2+sEVs group compared with the H_2O_2 group. GO analysis revealed that several genes, including those related to the cellular response to lipopolysaccharide, wound healing, and the positive regulation of ROS metabolic processes, were enriched in the H_2O_2+sEVs group (Fig. 6B). Moreover, GSEA revealed that TGFβ signaling and Kras signaling were closely related to H_2O_2+sEVs treatment and that the regulation of mitochondrial membrane permeability involved in the apoptotic process was related to H_2O_2 treatment (Fig. 6C). The above results demonstrated that H_2O_2 acted as a signaling molecule to activate DPSCs in response to OS and that DFSC-sEVs could exert regulatory effects on H_2O_2-stimulated DPSCs at the transcriptional level.

3.6. ***SA-RhB*** exhibits excellent injectability, ROS responsiveness, biocompatibility and loading capacity for DFSC-sEVs

To enhance the bioavailability and clinical efficacy of DFSC-sEVs, an injectable ROS-responsive hydrogel was constructed to load DFSC-sEVs. A schematic illustration of **SA-RhB**@sEVs is shown in Fig. 7A. **SA** crosslinked with Ca^{2+} was used as the first network, and the monomer **RhB-AC** was introduced as a ROS sensor. Finally, the double-layer IPN hydrogel **SA-RhB** was formed. SEM showed that both **SA** and **SA-RhB** exhibited porous internal structures and that the pores in **SA-RhB** were denser and smaller than those in **SA** (Fig. 7B). Na_2HPO_4 was used to interact with $CaSO_4$, thus slowing the crosslinking speed of **SA** and Ca^{2+}. As shown in Table S3, the gelation times differed among the different combinations of Na_2HPO_4 and $CaSO_4$, and 0.3 M Na_2HPO_4 combined with 1.52 M $CaSO_4$ was ultimately chosen to provide 3.50 ± 0.71 min of gelation for clinical operation.

As presented in Fig. 7C, **SA-RhB** slowly turned from a liquid to the solid-state within 4 min and subsequently formed a transparent, flexible and uniform hydrogel. In addition, the solution could be easily extruded from a syringe before gelation, suggesting the satisfactory injectability of **SA-RhB**. To estimate the specificity of the $HClO/ClO^-$ response, we first tested the fluorescence response of the monomer **RhB-AC** toward various ROS. Fluorescence spectroscopy revealed a significant fluorescence emission peak at 580 nm when **RhB-AC** was reacted with 100 μM $HClO/ClO^-$. However, the fluorescence could be slightly excited by $ONOO^-$ and was seldom excited by H_2O_2, ·OH, $^tBuOOH^-$ or O_2^- (Fig. S4A). The response of **SA-RhB** to $HClO/ClO^-$ was further studied. When **SA-RhB** was reacted with 50 μM $HClO/ClO^-$ for 1 min, slight fluorescence emission could be captured by 365 nm UV light or fluorescence spectroscopy; the fluorescence intensity increased as the treatment time increased or the $HClO/ClO^-$ concentration increased

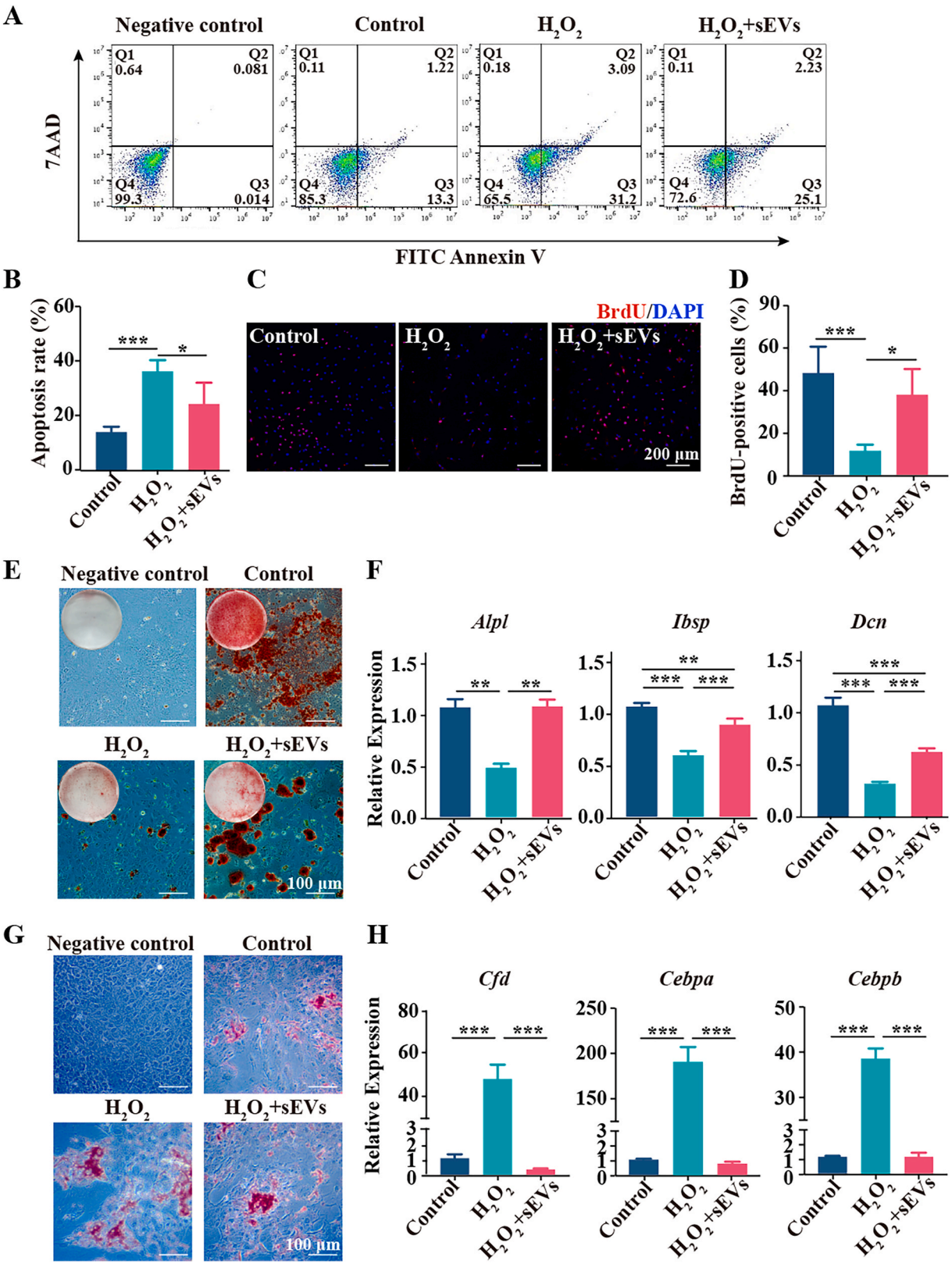

Fig. 3. DFSC-sEVs enhanced the survival, proliferation and osteogenesis/odontogenesis of H_2O_2-damaged DPSCs. (A) DPSCs apoptosis was examined by an Annexin V-FITC/7AAD assay. (B) Apoptosis rates of DPSCs, including early apoptosis (Annexin-V^+7AAD^-) and late apoptosis (Annexin-V^+7AAD^+). (C, D) Representative images of BrdU staining and quantification of DPSCs. (E) Representative images of alizarin red staining after osteogenic induction for 21 d. (F) qRT–PCR analysis of the mRNA expression of the odontogenesis-related factors *Alpl*, *Ibsp* and *Dcn*. (G) Representative images of Oil Red O staining after adipogenic induction for 21 d. (H) qRT–PCR analysis of the mRNA expression of the adipogenic-related factors *Cfd*, *Cebpa* and *Cebpb*. ***$P < 0.001$, **$P < 0.01$, *$P < 0.05$.

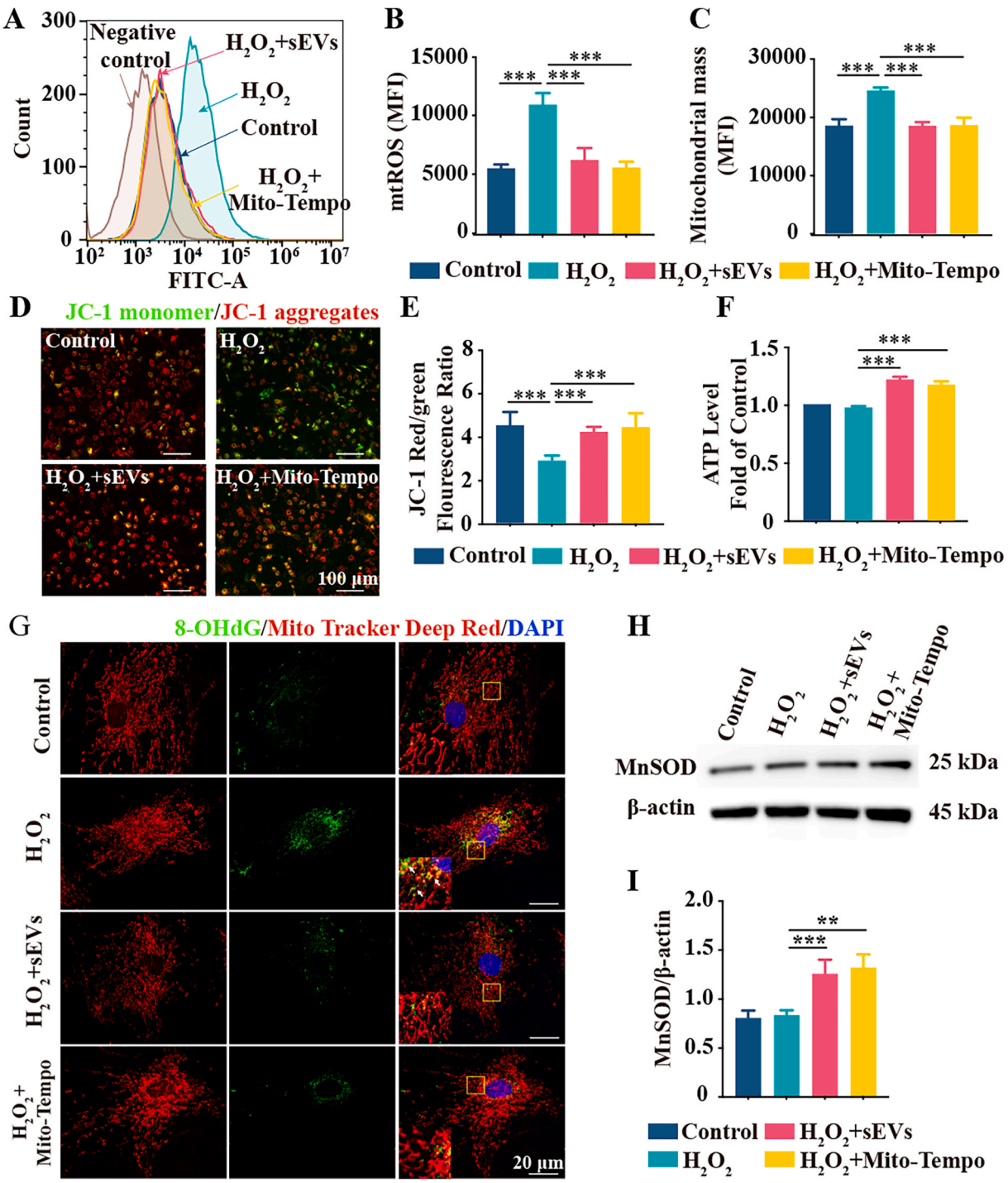

Fig. 4. DFSC-sEVs restored the mitochondrial dysfunction of H_2O_2-damaged DPSCs. (A, B) mtROS results for DPSCs (MitoSOX staining). (C) Mitochondrial mass was quantified by MitoTracker Green staining. (D) Representative images of JC-1 staining; JC-1 aggregates exhibit red fluorescence, and JC-1 monomers exhibit green fluorescence. (E) The ratio of the mean fluorescence intensity of JC-1 red to that of JC-1 green fluorescence. (F) ATP production was evaluated with an ATP kit. (G) Colocalization of 8-OHdG and MitoTracker Deep Red-labeled mitochondria in DPSCs. (H, I) Representative results from the Western blot analysis of MnSOD. MFI, mean fluorescence intensity. $^{***}P < 0.001$, $^{**}P < 0.01$.

(Fig. 7D and E). After reacting for 360 min, the accumulation of fluorescence at 580 nm tended to stabilize, as shown in Fig. 7E.

An *in vitro* degradation test revealed that in the presence of the calcium chelator EDTA and/or HClO/ClO$^-$, **SA-RhB** was susceptible to degradation, resulting in the sustained release of drugs loaded in **SA-RhB**. **SA-RhB** was degraded in a HClO/ClO$^-$ concentration-dependent manner, and the gel was completely degraded after soaking in 1000 μM HClO/ClO$^-$ for 3 d (Fig. S4B). In addition, the water retention capacity of the IPN hydrogel was evaluated. As shown in Fig. S4 C and D, **SA-RhB** lost almost 50 % of its weight after 5 h. Afterward, the hydrogel was soaked in PBS, after which the weight of **SA-RhB** slowly increased to its original mass after another 5 h. Furthermore, the swelling kinetics analysis revealed that the swelling ratio increased to almost 30 % after 60 min and then decreased to 20 % after 120 min (Fig. S4E).

Excellent biocompatibility is a prerequisite for pulp capping materials. Instead of interfering with DPSCs viability after 1 d, 2 d and 3 d,

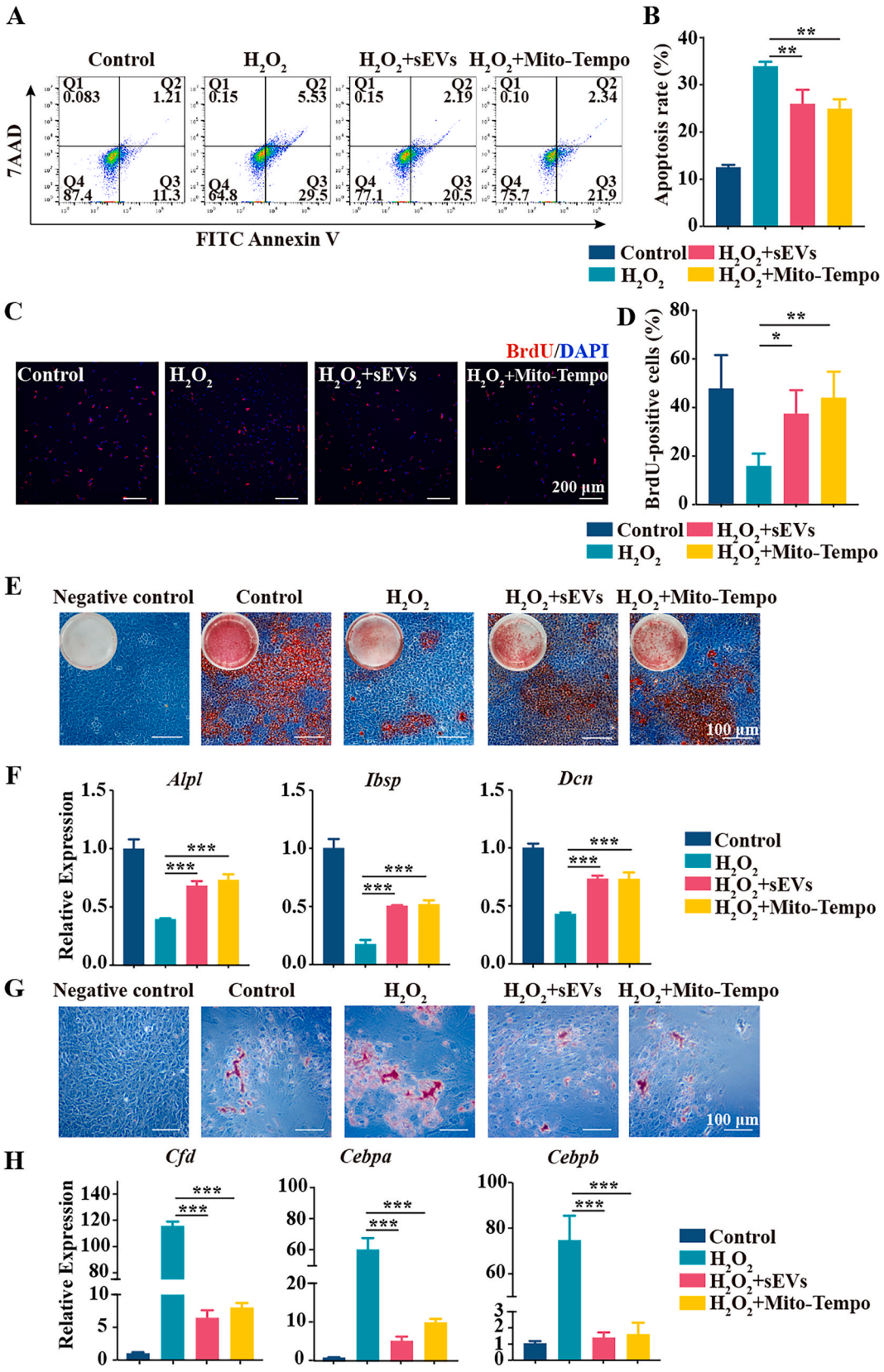

Fig. 5. DFSC-sEVs exerted cytoprotective effects on H_2O_2-induced damage by maintaining mitochondrial homeostasis. (A) DPSCs apoptosis was examined using an Annexin V-FITC/7AAD assay. (B) Apoptosis rates of DPSCs, including early apoptosis (Annexin-V^+7AAD^-) and late apoptosis (Annexin-V^+7AAD^+). (C, D) Representative images of BrdU staining and quantification of DPSCs. (E) Representative images of alizarin red staining after osteogenic induction for 21 d. (F) qRT−PCR analysis of the mRNA expression of the odontogenesis-related factors *Alpl*, *Ibsp* and *Dcn*. (G) Representative images of Oil Red O staining after adipogenic induction for 21 d. (H) qRT−PCR analysis of the mRNA expression of the adipogenic-related factors *Cfd*, *Cebpa* and *Cebpb*. $^{***}P < 0.001$, $^{**}P < 0.01$, $^{*}P < 0.05$.

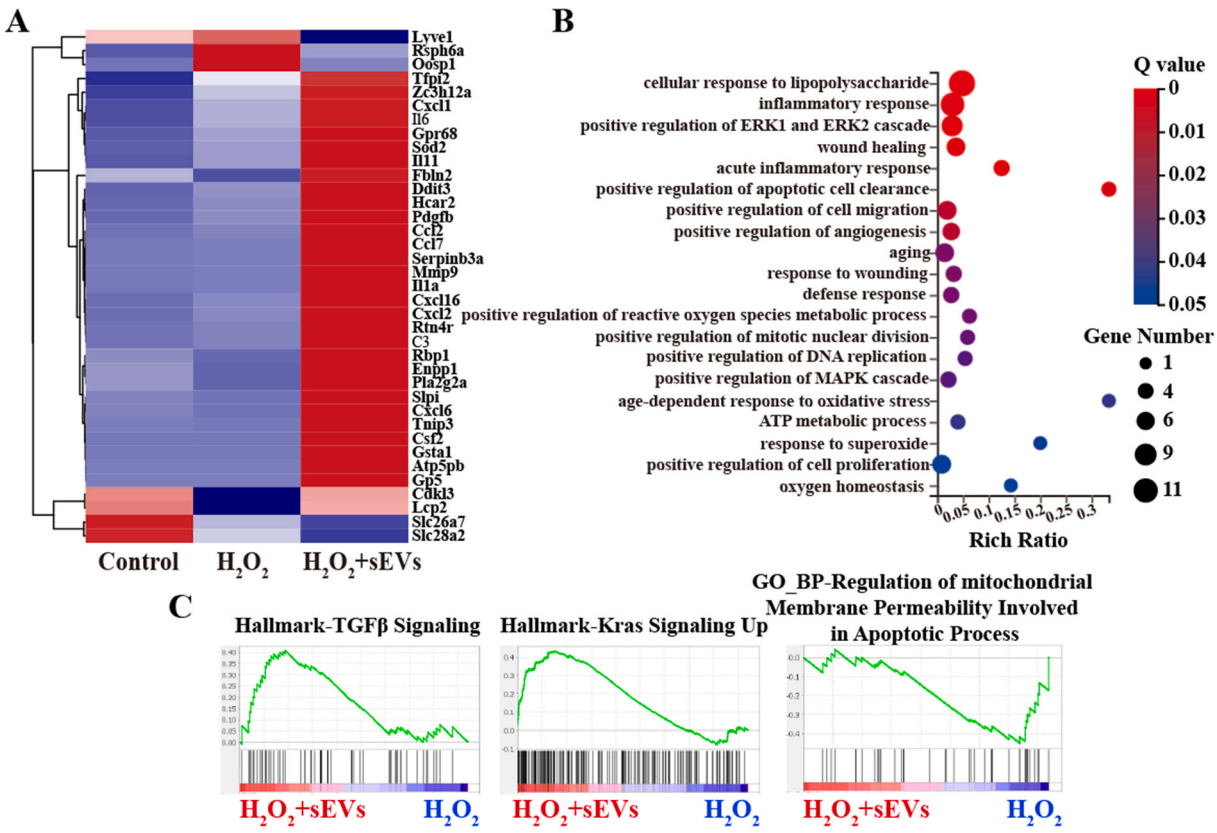

Fig. 6. DFSC-sEVs-mediated alterations in the transcriptional profile determined by RNA sequencing. (A) Heatmap of DEGs in the H_2O_2 group and H_2O_2+sEVs group according to the criteria of a fold change $\geq|2|$ and a *q* value < 0.5. (B) Biological process category of GO analysis of DEGs in the H_2O_2 group and H_2O_2+sEVs group. (C) Genes enriched in representative pathways according to GSEA.

0.1 mg/mL to 2 mg/mL **SA-RhB** degradation products led to a significant increase in proliferative activity to some extent, especially after 2 d (Fig. 7F). Live/dead staining also revealed that the viability of DPSCs was well preserved when they were cultured with the **SA-RhB** degradation products for 1 d, 2 d and 3 d (Fig. 7G, Fig. S4F). Next, the loading and release capacity of **SA-RhB** was assessed. Representative confocal z-stack images confirmed that a large amount of PKH67-labeled DFSC-sEVs were evenly encapsulated in **SA-RhB** (Fig. 7H). In addition, as shown in Fig. 7I, DFSC-sEVs loaded in **SA-RhB** (**SA-RhB**@sEVs) were continuously released in a concentration-dependent manner. HClO/ClO^- clearly increased the release rate, as 100 μM and 500 μM HClO/ClO^- resulted in the release of approximately 60 % of the DFSC-sEVs within 5 d, and the addition of 1000 μM HClO/ClO^- triggered the release of approximately 80 % of the DFSC-sEVs. The above results illustrated that **SA-RhB** exhibited excellent injectability, ROS responsiveness, biocompatibility and controlled release of DFSC-sEVs.

*3.7. DFSC-sEVs-loaded **SA-RhB** exhibits enhanced antioxidant and prohealing effects on inflamed pulp*

Finally, we investigated whether sEVs-loaded **SA-RhB** had better therapeutic effects than DFSC-sEVs soaked in a gelatin sponge on an experimental pulpitis model. Immunofluorescence staining showed that the use of **SA-RhB** alone attenuated OS in inflamed pulp compared with that in the LPS group but did not decrease the percentage of 8-$OHdG^+$ $CD90^+$ cells. However, the combination of **SA-RhB** and DFSC-sEVs reduced LPS-induced OS more effectively than **SA-RhB** or DFSC-sEVs alone and exhibited better antioxidative effects on $CD90^+$ cells (Fig. 8A–C). Furthermore, the expression of DSPP in the pulpal wound in the LPS + **SA-RhB**@sEVs group was higher than that in the LPS + sEVs group and the staining was more concentrated (Fig. 8 D). The histological analysis of the cells showed that **SA-RhB** alone failed to mitigate the level of LPS-induced inflammation at 3 d and 7 d. However, the incorporation of **SA-RhB** and DFSC-sEVs successfully resulted in less inflammation during the same duration and accelerated the resolution of inflammation compared with that in the LPS + sEVs group (Figs. S5A and B). At 28 d post-treatment, although both DFSC-sEVs and **SA-RhB**@sEVs induced thick reparative dentin layers to completely close the exposed site of the pulp, extensive calcification was observed in the LPS + sEVs group, an effect that was unexpected during pulp healing (Fig. 8F). The analysis of micro-CT image also revealed that the incorporation of **SA-RhB** and DFSC-sEVs significantly increased the BV/TV ratio at the pulp exposure site compared with that in the LPS + sEVs group (Figs. S5C and D). Taken together, these results indicated that the ROS-responsive hydrogel **SA-RhB** enhanced the antioxidant and reparative effects of DFSC-sEVs on LPS-induced pulpitis models.

4. Discussion

Excessive ROS are a typical inflammatory hallmark [20]. Conversely, highly reactive ROS also exacerbate inflammation by oxidizing cellular components and acting as proinflammatory signaling molecules [21]. In inflamed dental pulp, uncontrolled OS aggravates inflammation and decreases the efficiency of pulpal wound healing [7]. In conjunction with our prior research, we substantiated that capping with iRoot BP Plus, a prevalent calcium silicate-based capping material, cannot promote the sufficient recovery of inflamed or infectious dental pulp, consequently impeding the formation of a complete dentin bridge [19]. Similarly, a previous study has similarly reported that mineral trioxide aggregate (MTA), another type of clinically available capping material, is ineffective against experimentally induced pulpitis *in vivo* [4]. Furthermore, we revealed that the introduction of DFSC-sEVs may be a

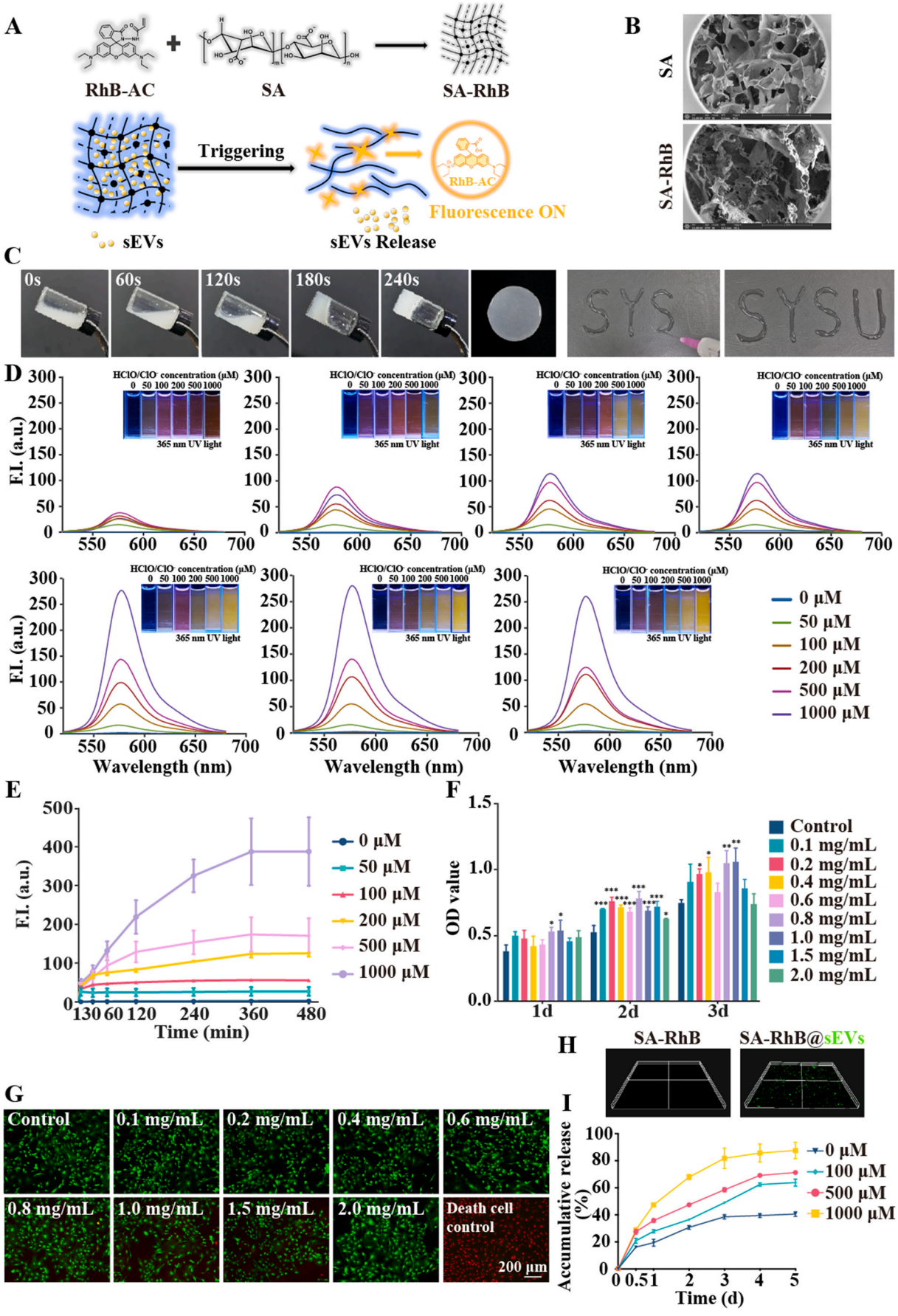

(caption on next page)

Fig. 7. Synthesis and characterization of SA-RhB and SA-RhB-incorporated DFSC-sEVs. (A) Flow chart for the synthesis of sEVs-loaded **SA-RhB**. (B) Representative SEM micrograph of the lyophilized hydrogel. (C) Optical images showing the gelation process and injectability of **SA-RhB**. (D) Fluorescence emission spectra of **SA-RhB** in different concentrations of $HClO/ClO^-$. (E) The mean fluorescence intensity (580 nm) of **SA-RhB** in response to $HClO/ClO^-$. (F) CCK-8 assay results showing the viability of DPSCs stimulated with **SA-RhB** degradation products for 1 d, 2 d and 3 d. (G) Representative images of live/dead staining of DPSCs stimulated with **SA-RhB** for degradation for 1 d. (H) The incorporation and distribution of PKH67-labeled DFSC-sEVs in **SA-RhB**. (I) Release kinetics of DFSC-sEVs from **SA-RhB** in response to $HClO/ClO^-$. FI, fluorescence intensity. $^{***}P < 0.001$, $^{**}P < 0.01$, $^{*}P < 0.05$.

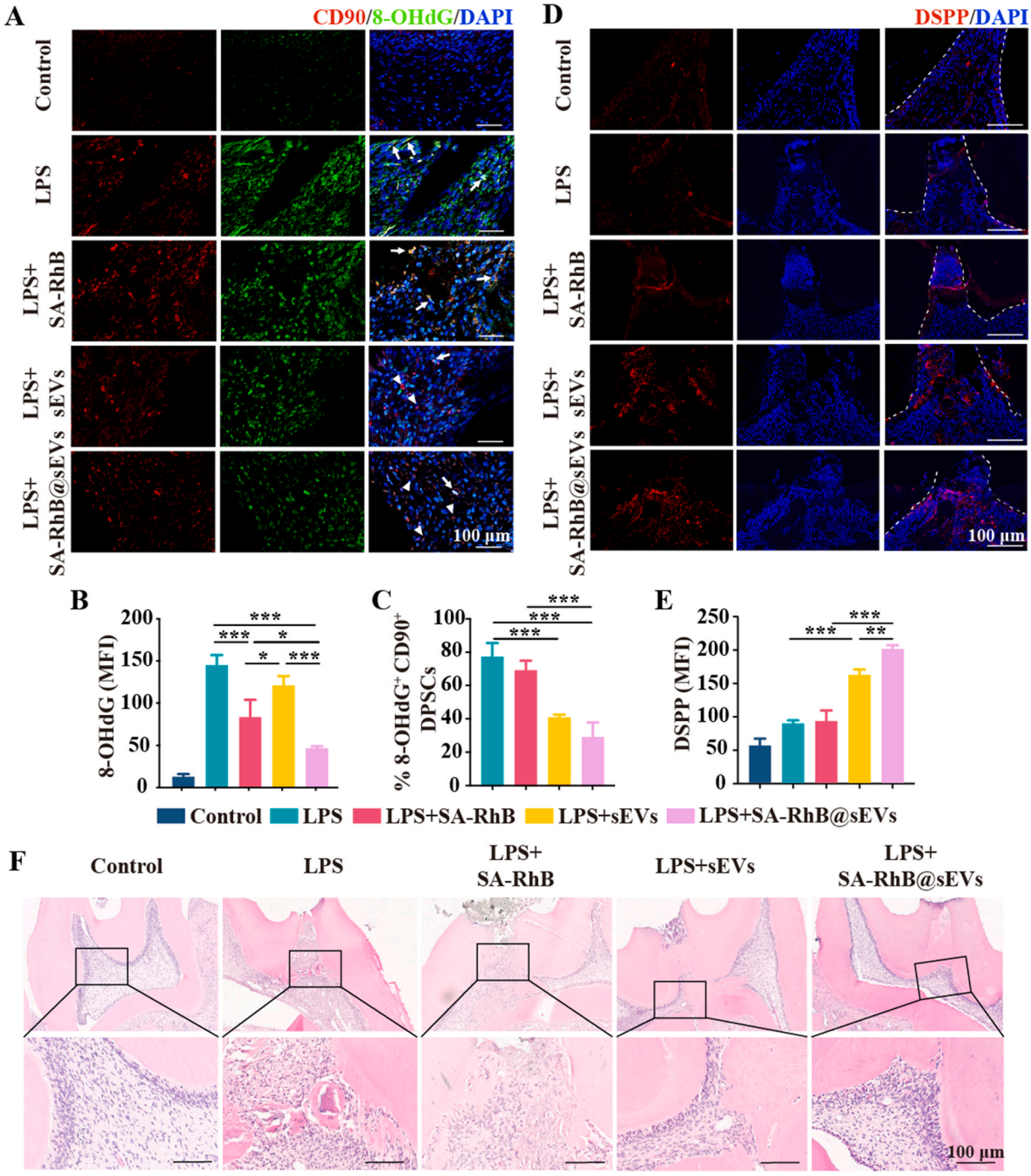

Fig. 8. DFSC-sEVs-loaded SA-RhB accelerated pulp healing. (A) Immunofluorescence staining for 8-OHdG and $CD90^+$ DPSCs at the site of pulp injury after treatment with **SA-RhB**@sEVs for 3 d. The arrows indicate $CD90^+$ DPSCs, and the arrowheads indicate $8\text{-}OHdG^+CD90^+$ DPSCs. (B, C) 8-OHdG expression and $CD90^+$ DPSCs exposed to oxidative stress 3 d after surgery. (D, E) DSPP expression at the pulp exposure site after treatment with **SA-RhB**@sEVs for 7 d. The white dashed lines indicate the junction between the dentin and dental pulp. (F) Representative histological images showing pulpal repair after treatment with **SA-RhB**@sEVs for 28 d. MFI, mean fluorescence intensity. $^{***}P < 0.001$, $^{**}P < 0.01$, $^{*}P < 0.05$.

useful strategy for effectively reducing OS in patients with pulpitis and promoting inflamed pulp repair. DFSCs are special dental stem cells isolated from the connective tissues surrounding the developing tooth germ that exhibit significantly greater proliferative activity and better immunomodulatory capacity than other dental stem cells [22]. Furthermore, DFSCs are abundant and easy to access. Several studies have shown that DFSCs can be advantageous for craniofacial bone and periodontal tissue regeneration [23–25]. Our previous study revealed that the conditioned medium of DFSCs could enhance the repair of LPS-induced pulpitis [17]. Therefore, DFSC-sEVs were isolated from the conditioned medium of DFSCs to evaluate their effects on inflamed pulp.

DPSCs in dental pulp tissues are a particular source of dentin regeneration and inflammation regulators [26,27]. We found that $CD90^+$ DPSCs suffered from remarkable OS in inflamed pulp, an effect that was reversed by DFSC-sEVs, suggesting that DFSC-sEVs might enhance the reparative potential of dental pulp by protecting DPSCs. To further elucidate the protective effect of DFSC-sEVs, an *in vitro* OS damage model was established by treating DPSCs with H_2O_2. It has been reported that MSCs, including DPSCs, are sensitive to high concentrations of H_2O_2 and subsequently undergo rapid apoptosis, thus exhibiting decreased proliferation and impaired osteogenic differentiation [28,29]. Here, we showed that DFSC-sEVs had a prominent protective effect on H_2O_2-treated DPSCs by restoring the oxidative/antioxidative balance, promoting cell survival and enhancing odontogenic differentiation. MSC-sEVs exert a variety of functions via direct/indirect pathways by delivering multiple biological molecules, including miRNAs, proteins, and DNA [30,31]. Previous studies have reported that MSC-sEVs can relieve OS by directly delivering antioxidant enzymes, such as SODs, catalase, and glutathione peroxidase. In addition, mRNAs, miRNAs and other signaling molecules involved in sEV uptake by recipient cells, can regulate downstream pathways involved in ROS production and antioxidative responses, including Keap1/Nrf2 and NOX4/p38 MAPK [10,14]. Our study showed that DFSC-sEVs could alleviate OS-induced DNA and lipid damage and increase SOD activity in DPSCs, but further studies are needed to determine the molecular mechanisms driving these effects. Interestingly, RNA sequencing further revealed that DFSC-sEVs not only improved the positive regulation of ROS metabolism but also promoted wound healing, TGFβ signaling and the ERK1/ERK2 cascade, indicating that multiple combinations of factors had synergistic effects on OS-damaged DPSCs.

Recently, the importance of mitochondria in contributing to MSCs redox homeostasis has been of great interest. Mitochondria are major producers of ROS, which increase susceptibility to OS damage [32]. Excessive mtROS accumulation leads to mitochondrial dysfunction and disturbs mitochondrial metabolism, in turn regulating cell fate [33,34]. Our study revealed that DFSC-sEVs exhibited effects similar to those of Mito-Tempo on reducing mtROS levels and the mitochondrial mass, upregulating the MMP and increasing ATP production, indicating that mitochondrial dysfunction in OS-injured DPSCs was alleviated. GSEA also revealed that the regulation of mitochondrial membrane permeability involved in the apoptotic process pathway was more enriched in the H_2O_2 group than in the H_2O_2+sEVs group. Furthermore, the ability of DFSC-sEVs to promote the survival and osteogenic/odontogenic differentiation of DPSCs undergoing OS was comparable to that of Mito-Tempo, while the potential cytotoxicity and side effects of synthetic antioxidant application could be avoided [35,36]. MSC-EVs can promote aged wound repair by alleviating mitochondrial dysfunction and reprogramming energy metabolism, and metformin-engineered MSC-EVs strengthened the therapeutic efficacy of MSC-EVs [37]. In addition, MSC-EVs mediated mitochondrial transfer can also restore mitochondrial functions in recipient cells [38]. These results suggested that mitochondria might be the major organelle through which DFSC-sEVs exert their protective effects on DPSCs.

Stem cells are prone to DNA oxidative damage because of their high proliferative activity [39,40]. We observed that DFSC-sEVs significantly decreased the percentage of 8-OHdG^+CD90^+ DPSCs in inflamed pulp and downregulated the expression of 8-OHdG in H_2O_2-treated DPSCs, confirming the protective effect of DFSC-sEVs on DNA oxidative damage. mtDNA lacks histones and is located close to the electron transport chain; therefore, mtDNA is more susceptible to oxidative damage than is nuclear DNA [41]. Conversely, mtDNA damage can lead to mtROS overproduction [42]. Thus, this vicious cycle contributes to aggravating mitochondrial dysfunction. Previous studies have reported that mtROS can promote mitochondrial dysfunction by suppressing mitochondrial transcription factor A (TFAM)-mediated mtDNA maintenance, while MSC-EVs can attenuate mtDNA damage in recipient cells by delivering TFAM mRNA [33,43]. In our study, both DFSC-sEVs and Mito-Tempo decreased the colocalization of 8-OHdG and MitoTracker Deep Red in H_2O_2-treated DPSCs, suggesting a reduction in oxidized mtDNA. In addition, the expression of the antioxidant MnSOD, which is an important ROS scavenger localized exclusively in mitochondria, was significantly upregulated by DFSC-sEVs. Therefore, DFSC-sEVs may protect DPSCs by reducing mtDNA oxidative damage and enhancing the mitochondrial antioxidant capacity, thereby alleviating mitochondrial OS.

Wound healing for pulpitis treatment is a dynamic and long-term process. MSC-sEVs can be rapidly cleared by macrophages *in vivo*, which may undermine the actual efficacy of sEV-based therapy [15]. Hence, various drug delivery systems have been developed to sustainably release sEVs. Inspired by the distinctive OS in pulpitis, we prepared a ROS-responsive IPN hydrogel composed of alginate and a ROS sensor to achieve the 'smart' release of DFSC-sEVs. IPN hydrogels enable two or more networks with different properties to establish a stable structure through topological entanglement and physical interactions, which can integrate the properties of each network and improve the functionality of the hydrogel [44]. Currently, the application of IPN hydrogel in dental pulp capping has rarely been reported. In this study, we constructed the monomer **RhB-AC** to efficiently respond to $HClO/ClO^-$, which is one of the most highly oxidative compounds and is usually generated during phagocytosis and the inflammatory response [45]. Excessive $HClO/ClO^-$ can react with various biomolecules, and result in various diseases, such as diabetic wounds, arthritis, cardiovascular disease, neurodegeneration, and even cancer [46]. In the pathological environment, the concentration of $HClO/ClO^-$ increases from the micromolar level to the millimolar level [47]. Therefore, accurately monitoring the fluctuations in $HClO/ClO^-$ is a promising method to assess tissue injuries. Our group is experienced in the design of hypochlorous acid-responding fluorescence sensors, and had previously synthesized a **RhB-AC** monomer with $HClO/ClO^-$ sensing/consuming properties [16,48,49]. Moreover, in contrast to broad-spectra ROS-responsive materials, the high selectivity of **RhB-AC** for $HClO/ClO^-$ provides a clear indication of $HClO/ClO^-$-related inflammatory activity, which could be more conducive to adjustable and predictable drug release kinetics. The present study showed that the monomer **RhB-AC** exhibited concentration- and time-dependent response behaviors, and that the IPN hydrogel **SA-RhB** efficiently decreased the oxidative damage of inflamed pulp *in vivo*. All these results corroborate the excellent ROS responsiveness of **RhB-AC.**

Moreover, alginate, which is a natural polysaccharide, was used to form an interpenetrating polymer network hydrogel with **RhB-AC.** Alginate has an excellent water content, biocompatibility and biodegradability, is nontoxic, has a soft consistency, and has been widely used as a MSC-sEVs delivery carrier for myocardial infarction, full-thickness skin wounds, diabetic wounds, etc. [50–52]. In this study, Na_2HPO_4 was used as a retarding agent to delay the interaction between **SA** and Ca^{2+}; thus, we increased the gelation time and facilitated clinical operation in a simple and inexpensive manner. In fact, this property of alginate has been widely applied to dental alginate impressions, which ensures excellent maneuverability in the clinic [53]. We further revealed that the **RhB-AC** crosslinked hydrogel **SA-RhB** was successfully constructed to efficiently upload and release DFSC-sEVs in a sustained manner. *In vivo* experiments showed that **SA-RhB** behaved as both a ROS scavenger and a ROS-responsive drug carrier. **SA-RhB** contributes to the

clearance of ROS in inflamed pulp, thus relieving the disruption of extracellular matrix homeostasis induced by OS. Moreover, DFSC-sEVs could be precisely released to protect OS-injured DPSCs. Furthermore, the incorporation of **SA-RhB** and DFSC-sEVs improved the therapeutic efficacy of the combination treatment in inflamed pulp via the synergistic effects of extracellular ROS consumption and the alleviation of intracellular OS. Therefore, this work provides a smart and effective ROS-responsive strategy for healing inflamed pulp.

P. gingivalis is a well-known periodontal pathogen that can invade the dental pulp through the channels within the periodontal pocket and has been detected in approximately 50 % of primary endodontic infections [54]. Therefore, in this study, *P. gingivalis*-derived LPS was used to induce similar and reproducible pulp inflammation in rat molars [55,56]. As the major pathogen-associated molecular pattern of gram-negative bacteria, LPS can be recognized by DPSCs, odontoblasts, fibroblasts and leukocytes, thus leading to an inflammatory response and subsequent pulp injury [57,58]. Using this well-established pulp injury model, we documented the preliminary *in vivo* efficacy of sEV-loaded ROS-responsive hydrogels in pulp repair following a gram-negative bacterial insult. Recently, a rat caries-induced pulpitis model has been reported for studies of vital pulp therapy, which more closely mimics clinical conditions [59]. Although this model requires a longer time course and shows great variability in caries progression, it may facilitate further exploration of the efficacy and effector molecules of DFSC-sEVs-based treatment.

5. Conclusions

DFSC-sEVs protected DPSCs against OS damage by regulating mitochondrial dysfunction, thus promoting the repair of inflamed pulp. In addition, the smart capping material **SA-RhB** was developed by incorporating DFSC-sEVs within a ROS-responsive hydrogel, which had synergistic therapeutic effects on the wound healing of inflamed pulp. Overall, **SA-RhB**@sEVs is a feasible MSC-sEVs-based therapy for vital pulp treatment of pulpitis.

Ethics approval and consent to participate

All animal procedures were approved by the Institutional Animal Care and Use Committee of Sun Yat-Sen University (Approval No. SYSU-IACUC-2021-000289).

CRediT authorship contribution statement

Mengjie Li: Writing – original draft, Methodology, Investigation, Formal analysis, Data curation. **Jun Tian:** Writing – original draft, Investigation, Funding acquisition, Data curation. **Kangkang Yu:** Writing – original draft, Methodology, Formal analysis. **He Liu:** Writing – original draft, Data curation. **Xiaoqi Yu:** Writing – review & editing, Conceptualization. **Nan Wang:** Methodology, Data curation. **Qimei Gong:** Writing – review & editing, Resources, Data curation. **Kun Li:** Writing – review & editing, Resources, Conceptualization. **Ya Shen:** Writing – review & editing, Supervision, Resources. **Xi Wei:** Writing – review & editing, Supervision, Project administration, Funding acquisition, Conceptualization.

Declaration of competing interest

Ya Shen is an associate editor for *Bioactive Materials* and was not involved in the editorial review or the decision to publish this article. He Liu is an editorial board member for *Bioactive Materials* and was not involved in the editorial review or the decision to publish this article. The authors declare that they have no known competing financial interests or personal relationships that could have appeared to influence the work reported in this paper.

Acknowledgments

This work was supported by the National Natural Science Foundation of China (No. 82370943, 82201037 and 81970925), the Young Elite Scientists Sponsorship Program by Guangzhou (QT-2023-030) and Fundamental Research Funds for the Central Universities, Sun Yat-sen University (23qnpy157).

Appendix A. Supplementary data

Supplementary data to this article can be found online at https://doi.org/10.1016/j.bioactmat.2024.06.036.

References

[1] H.F. Duncan, K.M. Galler, P.L. Tomson, S. Simon, I. El-Karim, R. Kundzina, G. Krastl, T. Dammaschke, H. Fransson, M. Markvart, M. Zehnder, L. Bjorndal, European Society of Endodontology position statement: management of deep caries and the exposed pulp, Int. Endod. J. 52 (2019) 923–934.

[2] H.F. Duncan, Y. Kobayashi, M. Kearney, E. Shimizu, Epigenetic therapeutics in dental pulp treatment: hopes, challenges and concerns for the development of next-generation biomaterials, Bioact. Mater. 27 (2023) 574–593.

[3] M. Li, X. Hu, X. Li, S. Lei, M. Cai, X. Wei, D. Deng, Dentist-related factors influencing the use of vital pulp therapy: a survey among dental practitioners in China, J. Int. Med. Res. 47 (2019) 2381–2393.

[4] D.H. Kim, J.H. Jang, B.N. Lee, H.S. Chang, I.N. Hwang, W.M. Oh, S.H. Kim, K. S. Min, J.T. Koh, Y.C. Hwang, Anti-inflammatory and mineralization effects of proroot mta and endocem mta in studies of human and rat dental pulps in vitro and in vivo, J. Endod. 44 (2018) 1534–1541.

[5] S. Shirawachi, K. Takeda, T. Naruse, Y. Takahasi, J. Nakanishi, S. Shindo, H. Shiba, Oxidative stress impairs the calcification ability of human dental pulp cells, BMC Oral Health 22 (2022) 437.

[6] H.D. Buzoglu, A. Burus, Y. Bayazit, M. Goldberg, Stem cell and oxidative stress-inflammation cycle, Curr. Stem Cell Res. Ther. 18 (2023) 641–652.

[7] H. Dogan Buzoglu, M. Ozcan, O. Bozdemir, K.S. Aydin Akkurt, N.D. Zeybek, Y. Bayazit, Evaluation of oxidative stress cycle in healthy and inflamed dental pulp tissue: a laboratory investigation, Clin. Oral Invest. 27 (2023) 5913–5923.

[8] V. Vengerfeldt, R. Mandar, M. Saag, A. Piir, T. Kullisaar, Oxidative stress in patients with endodontic pathologies, J. Pain Res. 10 (2017) 2031–2040.

[9] S. Huang, B. Zheng, X. Jin, Q. Yu, X. Zhang, X. Sun, Y. Chen, X. Ren, D. Wismeijer, J. Ma, C. Zhang, G. Wu, Y. Pan, Blockade of Cyclophilin D attenuates oxidative stress-induced cell death in human dental pulp cells, Oxid. Med. Cell. Longev. 2019 (2019) 1729013.

[10] J. Ma, X. Shi, M. Li, S. Chen, Q. Gu, J. Zheng, D. Li, S. Wu, H. Yang, X. Li, MicroRNA-181a-2-3p shuttled by mesenchymal stem cell-secreted extracellular vesicles inhibits oxidative stress in Parkinson's disease by inhibiting EGR1 and NOX4, Cell Death Dis. 8 (2022) 33.

[11] Z. Liu, Y. Zhuang, L. Fang, C. Yuan, X. Wang, K. Lin, Breakthrough of extracellular vesicles in pathogenesis, diagnosis and treatment of osteoarthritis, Bioact. Mater. 22 (2023) 423–452.

[12] C. Tu, H. Lu, T. Zhou, W. Zhang, L. Deng, W. Cao, Z. Yang, Z. Wang, X. Wu, J. Ding, F. Xu, C. Gao, Promoting the healing of infected diabetic wound by an anti-bacterial and nano-enzyme-containing hydrogel with inflammation-suppressing, ROS-scavenging, oxygen and nitric oxide-generating properties, Biomaterials 286 (2022) 121597.

[13] C. Thery, K.W. Witwer, E. Aikawa, M.J. Alcaraz, J.D. Anderson, R. Andriantsitohaina, A. Antoniou, T. Arab, F. Archer, G.K. Atkin-Smith, D.C. Ayre, J.M. Bach, D. Bachurski, H. Baharvand, L. Balaj, S. Baldacchino, N.N. Bauer, A. A. Baxter, M. Bebawy, C. Beckham, A. Bedina Zavec, A. Benmoussa, A.C. Berardi, P. Bergese, E. Bielska, C. Blenkiron, S. Bobis-Wozowicz, E. Boilard, W. Boireau, A. Bongiovanni, F.E. Borras, S. Bosch, C.M. Boulanger, X. Breakefield, A.M. Breglio, M.A. Brennan, D.R. Brigstock, A. Brisson, M.L. Broekman, J.F. Bromberg, P. Bryl-Gorecka, S. Buch, A.H. Buck, D. Burger, S. Busatto, D. Buschmann, B. Bussolati, E. I. Buzas, J.B. Byrd, G. Camussi, D.R. Carter, S. Caruso, L.W. Chamley, Y.T. Chang, C. Chen, S. Chen, L. Cheng, A.R. Chin, A. Clayton, S.P. Clerici, A. Cocks, E. Cocucci, R.J. Coffey, A. Cordeiro-da-Silva, Y. Couch, F.A. Coumans, B. Coyle, R. Crescitelli, M.F. Criado, C. D'Souza-Schorey, S. Das, A. Datta Chaudhuri, P. de Candia, E.F. De Santana, O. De Wever, H.A. Del Portillo, T. Demaret, S. Deville, A. Devitt, B. Dhondt, D. Di Vizio, L.C. Dieterich, V. Dolo, A.P. Dominguez Rubio, M. Dominici, M.R. Dourado, T.A. Driedonks, F.V. Duarte, H.M. Duncan, R. M. Eichenberger, K. Ekstrom, S. El Andaloussi, C. Elie-Caille, U. Erdbrugger, J. M. Falcon-Perez, F. Fatima, J.E. Fish, M. Flores-Bellver, A. Forsonits, A. Frelet-Barrand, F. Fricke, G. Fuhrmann, S. Gabrielsson, A. Gamez-Valero, C. Gardiner, K. Gartner, R. Gaudin, Y.S. Gho, B. Giebel, C. Gilbert, M. Gimona, I. Giusti, D. C. Goberdhan, A. Gorgens, S.M. Gorski, D.W. Greening, J.C. Gross, A. Gualerzi, G. N. Gupta, D. Gustafson, A. Handberg, R.A. Haraszti, P. Harrison, H. Hegyesi, A. Hendrix, A.F. Hill, F.H. Hochberg, K.F. Hoffmann, B. Holder, H. Holthofer, B. Hosseinkhani, G. Hu, Y. Huang, V. Huber, S. Hunt, A.G. Ibrahim, T. Ikezu, J. M. Inal, M. Isin, A. Ivanova, H.K. Jackson, S. Jacobsen, S.M. Jay, M. Jayachandran, G. Jenster, L. Jiang, S.M. Johnson, J.C. Jones, A. Jong, T. Jovanovic-Talisman, S. Jung, R. Kalluri, S.I. Kano, S. Kaur, Y. Kawamura, E.T. Keller, D. Khamari, E. Khomyakova, A. Khvorova, P. Kierulf, K.P. Kim, T. Kislinger, M. Klingeborn, D.

J. Klinke 2nd, M. Kornek, M.M. Kosanovic, A.F. Kovacs, E.M. Kramer-Albers, S. Krasemann, M. Krause, I.V. Kurochkin, G.D. Kusuma, S. Kuypers, S. Laitinen, S. M. Langevin, L.R. Languino, J. Lannigan, C. Lasser, L.C. Laurent, G. Lavieu, E. Lazaro-Ibanez, S. Le Lay, M.S. Lee, Y.X.F. Lee, D.S. Lemos, M. Lenassi, A. Leszczynska, I.T. Li, K. Liao, S.F. Libregts, E. Ligeti, R. Lim, S.K. Lim, A. Line, K. Linnemannstons, A. Llorente, C.A. Lombard, M.J. Lorenowicz, A.M. Lorincz, J. Lotvall, J. Lovett, M.C. Lowry, X. Loyer, Q. Lu, B. Lukomska, T.R. Lunavat, S. L. Maas, H. Malhi, A. Marcilla, J. Mariani, J. Mariscal, E.S. Martens-Uzunova, L. Martin-Jaular, M.C. Martinez, V.R. Martins, M. Mathieu, S. Mathivanan, M. Maugeri, L.K. McGinnis, M.J. McVey, D.G. Meckes Jr., K.L. Meehan, I. Mertens, V.R. Minciacchi, A. Moller, M. Moller Jorgensen, A. Morales-Kastresana, J. Morhayim, F. Mullier, M. Muraca, L. Musante, V. Mussack, D.C. Muth, K. H. Myburgh, T. Najrana, M. Nawaz, I. Nazarenko, P. Nejsum, C. Neri, T. Neri, R. Nieuwland, L. Nimrichter, J.P. Nolan, E.N. Nolte-'t Hoen, N. Noren Hooten, L. O'Driscoll, T. O'Grady, A. O'Loghlen, T. Ochiya, M. Olivier, A. Ortiz, L.A. Ortiz, X. Osteikoetxea, O. Ostergaard, M. Ostrowski, J. Park, D.M. Pegtel, H. Peinado, F. Perut, M.W. Pfaffl, D.G. Phinney, B.C. Pieters, R.C. Pink, D.S. Pisetsky, E. Pogge von Strandmann, I. Polakovicova, I.K. Poon, B.H. Powell, I. Prada, L. Pulliam, P. Quesenberry, A. Radeghieri, R.L. Raffai, S. Raimondo, J. Rak, M.I. Ramirez, G. Raposo, M.S. Rayyan, N. Regev-Rudzki, F.L. Ricklefs, P.D. Robbins, D. D. Roberts, S.C. Rodrigues, E. Rohde, S. Rome, K.M. Rouschop, A. Rughetti, A. E. Russell, P. Saa, S. Sahoo, E. Salas-Huenuleo, C. Sanchez, J.A. Saugstad, M. J. Saul, R.M. Schiffelers, R. Schneider, T.H. Schoyen, A. Scott, E. Shahaj, S. Sharma, O. Shatnyeva, F. Shekari, G.V. Shelke, A.K. Shetty, K. Shiba, P.R. Siljander, A. M. Silva, A. Skowronek, O.L. Snyder 2nd, R.P. Soares, B.W. Sodar, C. Soekmadji, J. Sotillo, P.D. Stahl, W. Stoorvogel, S.L. Stott, E.F. Strasser, S. Swift, H. Tahara, M. Tewari, K. Timms, S. Tiwari, R. Tixeira, M. Tkach, W.S. Toh, R. Tomasini, A. C. Torrecilhas, J.P. Tosar, V. Toxavidis, L. Urbanelli, P. Vader, B.W. van Balkom, S. G. van der Grein, J. Van Deun, M.J. van Herwijnen, K. Van Keuren-Jensen, G. van Niel, M.E. van Royen, A.J. van Wijnen, M.H. Vasconcelos, I.J. Vechetti Jr., T. D. Veit, L.J. Vella, E. Velot, F.J. Verweij, B. Vestad, J.L. Vinas, T. Visnovitz, K. V. Vukman, J. Wahlgren, D.C. Watson, M.H. Wauben, A. Weaver, J.P. Webber, V. Weber, A.M. Wehman, D.J. Weiss, J.A. Welsh, S. Wendt, A.M. Wheelock, Z. Wiener, L. Witte, J. Wolfram, A. Xagorari, P. Xander, J. Xu, X. Yan, M. Yanez-Mo, H. Yin, Y. Yuana, V. Zappulli, J. Zarubova, V. Zekas, J.Y. Zhang, Z. Zhao, L. Zheng, A.R. Zheutlin, A.M. Zickler, P. Zimmermann, A.M. Zivkovic, D. Zocco, E. K. Zuba-Surma, Minimal information for studies of extracellular vesicles 2018 (MISEV2018): a position statement of the International Society for Extracellular Vesicles and update of the MISEV2014 guidelines, J. Extracell. Vesicles 7 (2018) 1535750.

[14] W. Zhang, T. Wang, Y. Xue, B. Zhan, Z. Lai, W. Huang, X. Peng, Y. Zhou, Research progress of extracellular vesicles and exosomes derived from mesenchymal stem cells in the treatment of oxidative stress-related diseases, Front. Immunol. 14 (2023) 1238789.

[15] O.P. Wiklander, J.Z. Nordin, A. O'Loughlin, Y. Gustafsson, G. Corso, I. Mager, P. Vader, Y. Lee, H. Sork, Y. Seow, N. Heldring, L. Alvarez-Erviti, C.I. Smith, K. Le Blanc, P. Macchiarini, P. Jungebluth, M.J. Wood, S.E. Andaloussi, Extracellular vesicle in vivo biodistribution is determined by cell source, route of administration and targeting, J. Extracell. Vesicles 4 (2015) 26316.

[16] K. Yu, N. Wang, Y. Shan, K. Li, J. Tian, X. Yu, X. Wei, HClO/ClO−-indicative interpenetrating polymer network hydrogels as intelligent bioactive materials for wound healing, ACS Appl. Bio Mater. 3 (2020) 37–44.

[17] H. Hong, X. Chen, K. Li, N. Wang, M. Li, B. Yang, X. Yu, X. Wei, Dental follicle stem cells rescue the regenerative capacity of inflamed rat dental pulp through a paracrine pathway, Stem Cell Res. Ther. 11 (2020) 333.

[18] J. Tian, W. Chen, Y. Xiong, Q. Li, S. Kong, M. Li, C. Pang, Y. Qiu, Z. Xu, Q. Gong, X. Wei, Small extracellular vesicles derived from hypoxic preconditioned dental pulp stem cells ameliorate inflammatory osteolysis by modulating macrophage polarization and osteoclastogenesis, Bioact. Mater. 22 (2023) 326–342.

[19] Y. Qiu, J. Tian, S. Kong, Y. Feng, Y. Lu, L. Su, Y. Cai, M. Li, J. Chang, C. Yang, X. Wei, SrCuSi(4) O(10)/GelMA composite hydrogel-mediated vital pulp therapy: integrating antibacterial property and enhanced pulp regeneration activity, Adv. Healthcare Mater. 12 (2023) e2300546.

[20] Y. Dou, C. Li, L. Li, J. Guo, J. Zhang, Bioresponsive drug delivery systems for the treatment of inflammatory diseases, J. Contr. Release 327 (2020) 641–666.

[21] J. Liu, X. Han, T. Zhang, K. Tian, Z. Li, F. Luo, Reactive oxygen species (ROS) scavenging biomaterials for anti-inflammatory diseases: from mechanism to therapy, J. Hematol. Oncol. 16 (2023) 116.

[22] C. Yang, X.Y. Du, W. Luo, Clinical application prospects and transformation value of dental follicle stem cells in oral and neurological diseases, World J. Stem Cell. 15 (2023) 136–149.

[23] M. Rezai-Rad, J.F. Bova, M. Orooji, J. Pepping, A. Qureshi, F. Del Piero, D. Hayes, S. Yao, Evaluation of bone regeneration potential of dental follicle stem cells for treatment of craniofacial defects, Cytotherapy 17 (2015) 1572–1581.

[24] X. Wei, S. Guo, Q. Liu, L. Liu, F. Huo, Y. Wu, W. Tian, Dental follicle stem cells promote periodontal regeneration through periostin-mediated macrophage infiltration and reprogramming in an inflammatory microenvironment, Int. J. Mol. Sci. 24 (2023) 6353.

[25] S. Guo, J. Kang, B. Ji, W. Guo, Y. Ding, Y. Wu, W. Tian, Periodontal-derived mesenchymal cell sheets promote periodontal regeneration in inflammatory microenvironment, Tissue Eng. 23 (2017) 585–596.

[26] S. Gronthos, M. Mankani, J. Brahim, P.G. Robey, S. Shi, Postnatal human dental pulp stem cells (DPSCs) in vitro and in vivo, Proc. Natl. Acad. Sci. U.S.A. 97 (2000) 13625–13630.

[27] F. Li, X. Wang, J. Shi, S. Wu, W. Xing, Y. He, Anti-inflammatory effect of dental pulp stem cells, Front. Immunol. 14 (2023) 1284868.

[28] R. Prakash, E. Fauzia, A.J. Siddiqui, S.K. Yadav, N. Kumari, M.T. Shams, A. Naeem, P.P. Praharaj, M.A. Khan, S.K. Bhutia, M. Janowski, J. Boltze, S.S. Raza, Oxidative stress-induced autophagy compromises stem cell viability, Stem Cell. 40 (2022) 468–478.

[29] R.A. Denu, P. Hematti, Optimization of oxidative stress for mesenchymal stromal/stem cell engraftment, function and longevity, Free Radic. Biol. Med. 167 (2021) 193–200.

[30] G. Bodega, M. Alique, L. Puebla, J. Carracedo, R.M. Ramírez, Microvesicles: ROS scavengers and ROS producers, J. Extracell. Vesicles 8 (2019) 1626654.

[31] Y. Zhuang, M. Cheng, M. Li, J. Cui, J. Huang, C. Zhang, J. Si, K. Lin, H. Yu, Small extracellular vesicles derived from hypoxic mesenchymal stem cells promote vascularized bone regeneration through the miR-210-3p/EFNA3/PI3K pathway, Acta Biomater. 150 (2022) 413–426.

[32] R.P. Chakrabarty, N.S. Chandel, Mitochondria as signaling organelles control mammalian stem cell fate, Cell Stem Cell 28 (2021) 394–408.

[33] M. Zhao, Y. Wang, L. Li, S. Liu, C. Wang, Y. Yuan, G. Yang, Y. Chen, J. Cheng, Y. Lu, J. Liu, Mitochondrial ROS promote mitochondrial dysfunction and inflammation in ischemic acute kidney injury by disrupting TFAM-mediated mtDNA maintenance, Theranostics 11 (2021) 1845–1863.

[34] J. Sun, F. Yang, L. Wang, H. Yu, Z. Yang, J. Wei, K. Vasilev, X. Zhang, X. Liu, Y. Zhao, Delivery of coenzyme Q10 loaded micelle targets mitochondrial ROS and enhances efficiency of mesenchymal stem cell therapy in intervertebral disc degeneration, Bioact. Mater. 23 (2023) 247–260.

[35] B. Halliwell, Understanding mechanisms of antioxidant action in health and disease, Nat. Rev. Mol. Cell Biol. 25 (2024) 13–33.

[36] B. Poljsak, D. Šuput, I. Milisav, Achieving the balance between ROS and antioxidants: when to use the synthetic antioxidants, Oxid. Med. Cell. Longev. 2013 (2013) 956792.

[37] Y. Zhuang, S. Jiang, X. Deng, A. Lao, X. Hua, Y. Xie, L. Jiang, X. Wang, K. Lin, Energy metabolism as therapeutic target for aged wound repair by engineered extracellular vesicle, Sci. Adv. 10 (2024) eadl0372.

[38] J. Dutra Silva, Y. Su, C.S. Calfee, K.L. Delucchi, D. Weiss, D.F. McAuley, C. O'Kane, A.D. Krasnodembskaya, Mesenchymal stromal cell extracellular vesicles rescue mitochondrial dysfunction and improve barrier integrity in clinically relevant models of ARDS, Eur. Respir. J. 58 (2021).

[39] T. Thalheim, M. Herberg, J. Galle, Linking DNA damage and age-related promoter dna hyper-methylation in the intestine, Genes 9 (2018).

[40] M. Valverde, J. Lozano-Salgado, P. Fortini, M.A. Rodriguez-Sastre, E. Rojas, E. Dogliotti, Hydrogen peroxide-induced dna damage and repair through the differentiation of human adipose-derived mesenchymal stem cells, Stem Cell. Int. 2018 (2018) 1615497.

[41] S.A. Madsen-Bouterse, G. Mohammad, M. Kanwar, R.A. Kowluru, Role of mitochondrial DNA damage in the development of diabetic retinopathy, and the metabolic memory phenomenon associated with its progression, Antioxidants Redox Signal. 13 (2010) 797–805.

[42] F.J. Blanco, A.M. Valdes, I. Rego-Pérez, Mitochondrial DNA variation and the pathogenesis of osteoarthritis phenotypes, Nat. Rev. Rheumatol. 14 (2018) 327–340.

[43] M. Zhao, S. Liu, C. Wang, Y. Wang, M. Wan, F. Liu, M. Gong, Y. Yuan, Y. Chen, J. Cheng, Y. Lu, J. Liu, Mesenchymal stem cell-derived extracellular vesicles attenuate mitochondrial damage and inflammation by stabilizing mitochondrial DNA, ACS Nano 15 (2021) 1519–1538.

[44] J. Wu, W. Xue, Z. Yun, Q. Liu, X. Sun, Biomedical applications of stimuli-responsive "smart" interpenetrating polymer network hydrogels, Mater. Today Bio. 25 (2024) 100998.

[45] G.J. Mao, Z.Z. Liang, J. Bi, H. Zhang, H.M. Meng, L. Su, Y.J. Gong, S. Feng, G. Zhang, A near-infrared fluorescent probe based on photostable Si-rhodamine for imaging hypochlorous acid during lysosome-involved inflammatory response, Anal. Chim. Acta 1048 (2019) 143–153.

[46] Q. Zhang, X. Hu, X. Dai, P. Ling, J. Sun, H. Chen, F. Gao, General strategy to achieve color-tunable ratiometric two-photon integrated single semiconducting polymer dot for imaging hypochlorous acid, ACS Nano 15 (2021) 13633–13645.

[47] S. Dong, L. Zhang, Y. Lin, C. Ding, C. Lu, Luminescent probes for hypochlorous acid in vitro and in vivo, Analyst 145 (2020) 5068–5089.

[48] K. Li, J.T. Hou, J. Yang, X.Q. Yu, A tumor-specific and mitochondria-targeted fluorescent probe for real-time sensing of hypochlorite in living cells, Chem. Commun. 53 (2017) 5539–5541.

[49] M. Li, K. Li, Y. Liu, H. Zhang, K. Yu, X. Liu, X. Yu, Mitochondria-immobilized fluorescent probe for the detection of hypochlorite in living cells, tissues, and zebrafishes, Anal. Chem. 92 (2020) 3262–3269.

[50] K. Lv, Q. Li, L. Zhang, Y. Wang, Z. Zhong, J. Zhao, X. Lin, J. Wang, K. Zhu, C. Xiao, C. Ke, S. Zhong, X. Wu, J. Chen, H. Yu, W. Zhu, X. Li, B. Wang, R. Tang, J. Wang, J. Huang, X. Hu, Incorporation of small extracellular vesicles in sodium alginate hydrogel as a novel therapeutic strategy for myocardial infarction, Theranostics 9 (2019) 7403–7416.

[51] S. Shafei, M. Khanmohammadi, R. Heidari, H. Ghanbari, V. Taghdiri Nooshabadi, S. Farzamfar, M. Akbariqomi, N.S. Sanikhani, M. Absalan, G. Tavoosidana, Exosome loaded alginate hydrogel promotes tissue regeneration in full-thickness skin wounds: an in vivo study, J. Biomed. Mater. Res. A. 108 (2020) 545–556.

[52] S. Guo, S. Tao, W. Yin, X. Qi, T. Yuan, C. Zhang, Exosomes derived from platelet-rich plasma promote the re-epithelization of chronic cutaneous wounds via activation of YAP in a diabetic rat model, Theranostics 7 (2017) 81–96.

[53] K.Y. Lee, D.J. Mooney, Alginate: properties and biomedical applications, Prog. Polym. Sci. 37 (2012) 106–126.

[54] B.P. Gomes, F. Montagner, R.C. Jacinto, A.A. Zaia, C.C. Ferraz, F.J. Souza-Filho, Polymerase chain reaction of Porphyromonas gingivalis, Treponema denticola, and

Tannerella forsythia in primary endodontic infections, J. Endod. 33 (2007) 1049–1052.
[55] R. Richert, M. Ducret, B. Alliot-Licht, M. Bekhouche, S. Gobert, J.C. Farges, A critical analysis of research methods and experimental models to study pulpitis, Int. Endod. J. 55 (Suppl 1) (2022) 14–36.
[56] M. Li, J. Tian, Z. Xu, Q. Zeng, W. Chen, S. Lei, X. Wei, Histology-based profile of inflammatory mediators in experimentally induced pulpitis in a rat model: screening for possible biomarkers, Int. Endod. J. 54 (2021) 1328–1341.
[57] E. Renard, A. Gaudin, G. Bienvenu, J. Amiaud, J.C. Farges, M.C. Cuturi, A. Moreau, B. Alliot-Licht, Immune cells and molecular networks in experimentally induced pulpitis, J. Dent. Res. 95 (2016) 196–205.
[58] J.H. Jang, H.W. Shin, J.M. Lee, H.W. Lee, E.C. Kim, S.H. Park, An overview of pathogen recognition receptors for innate immunity in dental pulp, Mediat. Inflamm. 2015 (2015) 794143.
[59] H. Huang, M. Okamoto, M. Watanabe, S. Matsumoto, K. Moriyama, S. Komichi, M. Ali, S. Matayoshi, R. Nomura, K. Nakano, Y. Takahashi, M. Hayashi, Development of rat caries-induced pulpitis model for vital pulp therapy, J. Dent. Res. 102 (2023) 574–582.